12-12-2023

Master Transcription Factor Reprogramming Unleashes Selective Translation Promoting Castration Resistance and Immune Evasion in Lethal Prostate Cancer

Sandra Santasusagna

Shijia Zhu

Vijayakumar Jawalagatti

Marc Carceles-Cordon

Adam Ertel

See next page for additional authors

Authors

Sandra Santasusagna, Shijia Zhu, Vijayakumar Jawalagatti, Marc Carceles-Cordon, Adam Ertel, Saioa Garcia-Longarte, Won-Min Song, Naoto Fujiwara, Peiyao Li, Isabel Mendizabal, Daniel P. Petrylak, William Kevin Kelly, E. Premkumar Reddy, Liguo Wang, Matthew J. Schiewer, Amaia Lujambio, Jeffrey Karnes, Karen E. Knudsen, Carlos Cordon-Cardo, Haidong Dong, Haojie Huang, Arkaitz Carracedo, Yujin Hoshida, Veronica Rodriguez-Bravo, and Josep Domingo-Domenech

RESEARCH ARTICLE

Master Transcription Factor Reprogramming Unleashes Selective Translation Promoting Castration Resistance and Immune Evasion in Lethal Prostate Cancer

Sandra Santasusagna[1,2], Shijia Zhu[3,4], Vijayakumar Jawalagatti[1,2], Marc Carceles-Cordon[1], Adam Ertel[5], Saioa Garcia-Longarte[6], Won-Min Song[7], Naoto Fujiwara[3], Peiyao Li[5], Isabel Mendizabal[6], Daniel P. Petrylak[8], William Kevin Kelly[5], E. Premkumar Reddy[9], Liguo Wang[2], Matthew J. Schiewer[10], Amaia Lujambio[9], Jeffrey Karnes[1], Karen E. Knudsen[10], Carlos Cordon-Cardo[11], Haidong Dong[1,12], Haojie Huang[1,2], Arkaitz Carracedo[6,13,14,15,16], Yujin Hoshida[3], Veronica Rodriguez-Bravo[1,2], and Josep Domingo-Domenech[1,2]

ABSTRACT Signaling rewiring allows tumors to survive therapy. Here we show that the decrease of the master regulator microphthalmia transcription factor (MITF) in lethal prostate cancer unleashes eukaryotic initiation factor 3B (eIF3B)–dependent translation reprogramming of key mRNAs conferring resistance to androgen deprivation therapy (ADT) and promoting immune evasion. Mechanistically, MITF represses through direct promoter binding *eIF3B*, which in turn regulates the translation of specific mRNAs. Genome-wide eIF3B enhanced cross-linking immunoprecipitation sequencing (eCLIP-seq) showed specialized binding to a UC-rich motif present in subsets of 5′ untranslated regions. Indeed, translation of the androgen receptor and major histocompatibility complex I (MHC-I) through this motif is sensitive to eIF3B amount. Notably, pharmacologic targeting of eIF3B-dependent translation in preclinical models sensitizes prostate cancer to ADT and anti–PD-1 therapy. These findings uncover a hidden connection between transcriptional and translational rewiring promoting therapy-refractory lethal prostate cancer and provide a druggable mechanism that may transcend into effective combined therapeutic strategies.

SIGNIFICANCE: Our study shows that specialized eIF3B-dependent translation of specific mRNAs released upon downregulation of the master transcription factor MITF confers castration resistance and immune evasion in lethal prostate cancer. Pharmacologic targeting of this mechanism delays castration resistance and increases immune-checkpoint efficacy.

INTRODUCTION

Cancer cells can dynamically respond and adapt to therapy by reprogramming their signaling cascades (1, 2). An example of this response is found in prostate cancer, a leading cause of cancer death in men worldwide (3). A variety of therapies are currently available for prostate cancer, including androgen deprivation therapy (ADT), chemotherapy (docetaxel, cabazitaxel), radium 223, sipuleucel-T, and antiandrogen therapy with abiraterone and enzalutamide, among others (4). Despite these therapeutic efforts, most patients' tumors invariably progress toward a drug-resistant state driven by a series of key molecular signaling events (4–6). The study of these altered rewiring signaling cascades that drive and sustain drug resistance offers the opportunity to identify actionable targets that can improve the survival of patients.

In this context, recent years have witnessed the discovery of several master transcription factors that enhance lethal prostate cancer aggressiveness and confer resistance to therapy (4). These factors share several features, such as the fact that they are at the top of a gene regulation hierarchy, their unaltered function as master regulators is indispensable in developmental programs and lineage acquisition, and when disrupted they can drive malignancies in more than one organ indicating their pan-cancer-promoting nature. As an example, the microphthalmia-associated transcription factor (MITF), which acts by binding to E-box motifs and contains a DNA-binding basic helix–loop–helix leucine zipper (bHLH-Zip) as well as a dimerization motif, which allows homo- or heterodimerization with members of the "Mi" transcription family (7), has a main role in the pathogenesis of multiple tumor types. "Mi" transcription family members, such as TFE3 and TFEB, participate in the pathogenesis of a subgroup of renal cell carcinomas (8, 9), whereas MITF is key in melanocyte development (7, 10, 11) and also

[1]Department of Urology, Mayo Comprehensive Cancer Center, Rochester, Minnesota. [2]Department of Biochemistry and Molecular Biology, Mayo Comprehensive Cancer Center, Rochester, Minnesota. [3]Department of Medicine, Simmons Comprehensive Cancer Center, University of Texas Southwestern Medical Center, Dallas, Texas. [4]Department of Laboratory Medicine and Pathology, University of Minnesota, Minneapolis, Minnesota. [5]Department of Oncology, Sidney Kimmel Cancer Center, Thomas Jefferson University, Philadelphia, Pennsylvania. [6]Center for Cooperative Research in Biosciences (CIC bioGUNE), Basque Research and Technology Alliance (BRTA), Derio, Spain. [7]Department of Genetics and Genome Sciences, Tisch Cancer Center, Icahn School of Medicine at Mount Sinai, New York, New York. [8]Department of Oncology, Yale Comprehensive Cancer Center, Yale School of Medicine, New Haven, Connecticut. [9]Department of Oncological Sciences, Tisch Cancer Center, Icahn School of Medicine at Mount Sinai, New York, New York. [10]Department of Pharmacology, Physiology, and Cancer Biology, Sidney Kimmel Cancer Center, Thomas Jefferson University, Philadelphia, Pennsylvania. [11]Department of Pathology. Tisch Cancer Center, Icahn School of Medicine at Mount Sinai, New York, New York. [12]Department of Immunology, Mayo Comprehensive Cancer Center, Rochester, Minnesota. [13]Ikerbasque, Basque Foundation for Science, Bilbao, Spain. [14]Traslational prostate cancer Research Lab, CIC bioGUNE-Basurto, Biocruces Bizkaia Health Research Institute CIC bioGUNE, Bizkaia Technology Park, Derio, Spain. [15]CIBERONC, Madrid, Spain. [16]Biochemistry and Molecular Biology Department, University of the Basque Country (UPV/EHU), Bilbao, Spain.

Note: S. Santasusagna, S. Zhu, and V. Jawalagatti contributed equally to this article.

Corresponding Authors: Josep Domingo-Domenech, Mayo Clinic, 200 First Street SW, Rochester, MN 55905. E-mail: domingo-domenech.josep@mayo.edu; Veronica Rodriguez-Bravo, Mayo Clinic, 200 First Street SW, Rochester, MN 55905. E-mail: rodriguezbravo.veronica@mayo.edu; Yujin Hoshida, University of Texas Southwestern Medical Center, 5323 Harry Hines Boulevard, Dallas, TX 75390. E-mail: Yujin.Hoshida@UTSouthwestern.edu

Cancer Discov 2023;13:2584–609

doi: 10.1158/2159-8290.CD-23-0306

contributes to melanoma. In melanoma, MITF behaves as an oncogene when amplified (12) and facilitates melanoma invasiveness (13, 14) and therapy resistance (15, 16) when MITF levels are low. In addition, MITF plays a role in the survival and growth of clear cell sarcoma (17) and pancreatic cancer (18). In prostate cancer, MITF through the regulation of the heat-shock protein CRYAB has been suggested to suppress tumor initiation (19). However, the role of MITF in advanced therapy-resistant lethal stages of the disease remains unknown.

Changes in the cell proteome derived from translational deregulation are an adaptive dynamic mechanism that allows survival of the tumor cells to therapy (20). As such, translational control is an increasingly important hallmark of tumorigenesis (21, 22), and there is evidence demonstrating that translation regulation by eIF4 subunits is a converging point downstream of the oncogenic PI3–AKT–mTOR, MYC, and MAPK signaling cascades in multiple human cancers (21, 23–25). In prostate cancer, eIF4 phosphorylation and subsequent dysregulation have been identified as a cause of pathogenesis (26–28), and 4E-BP1 has been linked to initiation and maintenance of prostate cancer as an effector of the PI3K–AKT–mTOR signaling pathway (29, 30). Moreover, the androgen receptor (AR) inhibits translation initiation through direct 4E-BP1 transcriptional regulation and AR loss results in increased translation, facilitating tumor cell proliferation (31). Nevertheless, the contribution of distinct subunits of the translation initiation complex to therapy resistance in prostate cancer remains poorly understood. For example, eukaryotic initiation factor 3B (eIF3B), a core subunit of the eIF3 translation initiation complex (32), is frequently overexpressed in prostate cancer (33), yet its contribution to lethal prostate cancer pathobiology remains unknown. Importantly, recent studies suggest that eIF3 subunits, including eIF3B, contribute to organism development and iron metabolism by both enhancing and repressing the translation of specific mRNAs (34–37). Thus, current evidence pinpoints toward an unexplored and potentially relevant role of eIF3B in prostate cancer.

In this study, we report that the MITF–eIF3B signaling axis confers therapy resistance to lethal prostate cancer. MITF is most significantly downregulated in advanced therapy-resistant prostate cancer when compared with normal and primary prostate cancer. Mechanistically, MITF represses the transcription of *eIF3B*, which, in turn when MITF levels decrease, affects via mRNA 5′ untranslated region (5′ UTR) binding on the translation of specific molecules, including AR and MHC-I, conferring castration resistance and immune evasion. Notably, pharmacologic reprogramming of eIF3B-dependent translation sensitizes prostate cancer to ADT and anti–PD-1 therapy in patient-derived and syngenic mouse cell preclinical models. Collectively, these results define an actionable signaling rewiring axis that copes on both transcriptional and translational mechanisms, enabling tumor cells to survive therapy exposure and progress to lethal stages of the disease.

RESULTS

MITF Downregulation Boosts the Aggressiveness of Advanced Lethal Prostate Cancer

To identify understudied mechanisms that may contribute to the progression of lethal prostate cancer, we interrogated the expression of 438 previously defined master transcription factors (38) in three publicly available patient datasets representing the transcriptome of primary and advanced therapy-resistant prostate cancer samples (39–41). This analysis confirmed the overexpression of several previously reported master transcription factors implicated in disease progression to lethal stages, such as ONECUT2 (42), FOXM1 (43), and GATA2 (44), as well as identified a subset of master transcription factors (TF) that decrease when comparing primary prostate cancer to advanced therapy-refractory disease stages (Fig. 1A and B; Supplementary Table S1).

Based on the fact that MITF is a top master TF consistently downregulated in the three datasets, together with recent publications suggesting that MITF represses early prostate cancer tumorigenesis (19) and may also play a role in advanced drug-tolerant prostate cancer (44), we decided to further investigate in detail the involvement of MITF downregulation in advanced lethal stages of the disease. Initially, to further define the clinical significance of MITF in the natural history of prostate cancer, we interrogated MITF expression levels in the three publicly available datasets and observed that *MITF* mRNA levels are most significantly decreased in advanced lethal prostate tumors when compared with both normal prostate and primary prostate cancer (Supplementary Fig. S1A). This result was confirmed when evaluating MITF protein expression in a cohort of 53 primary and 20 lethal metastatic castration-resistant prostate cancer tissue samples (Fig. 1C). Moreover, when analyzing MITF protein expression in the 53 primary prostate cancer tissue samples, we observed a significant association between low MITF expression and high Gleason score, a well-established pathologic characteristic of primary prostate cancer aggressiveness (Supplementary Fig. S1B). This association between MITF expression and Gleason score was also observed at the mRNA level in

Figure 1. MITF expression is downregulated in advanced lethal prostate cancer patient samples. **A,** Heat maps of master transcription factor (TF) gene expression in indicated publicly available datasets (GSE35988, GSE3933, and GSE21032). The value in the heat map refers to the color bar. The bar plot shows the signed $-\log_{10} P$ values of the *t* test by comparing advanced/autopsy to primary prostate cancer. The bar marked in red highlights *MITF*. **B,** Venn diagram of upregulated and downregulated master TFs ($P < 0.01$) among three publicly available datasets. Top 10 commonly deregulated master TFs including at least 2 patient datasets are listed. **C,** Representative MITF IHC and quantification of MITF-positive cells in morphologically normal prostate glands from prostatectomy specimens, primary prostate cancer, and advanced prostate cancer. PCa, prostate cancer. Scale bar, 100 μm. **D,** Disease-free survival based on MITF protein expression in a cohort of 52 patients with primary prostate cancer with clinical follow-up. The MITF cutoff point was low ≤20% and high >20% MITF nuclear staining positive cells. **E,** Disease-free survival based on *MITF* mRNA expression in patients with primary prostate cancer from two publicly available datasets with clinical follow-up (GSE21032 and https://www.cancer.gov/tcga). The optimal cutoff point was selected automatically using the surv_cutpoint method from the survminer package in R/Bioconductor. TCGA, The Cancer Genome Atlas. *, $P < 0.05$.

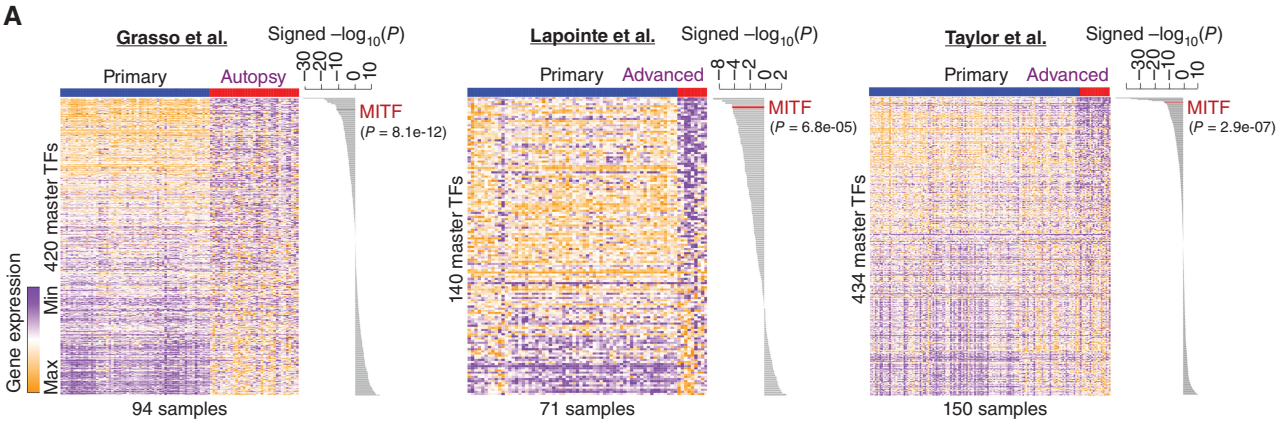

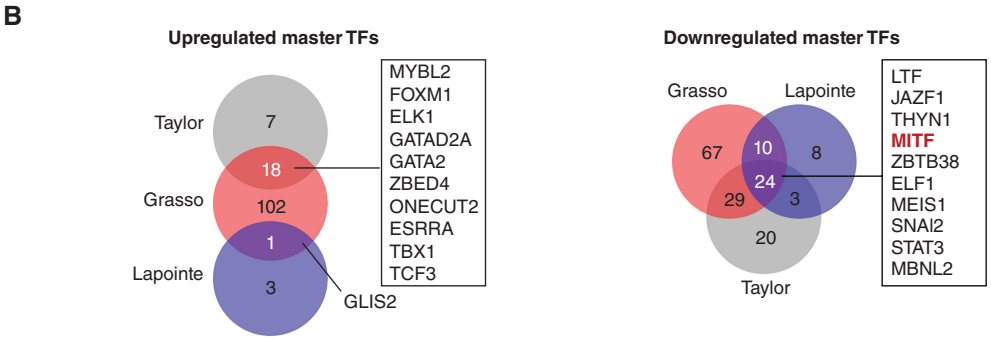

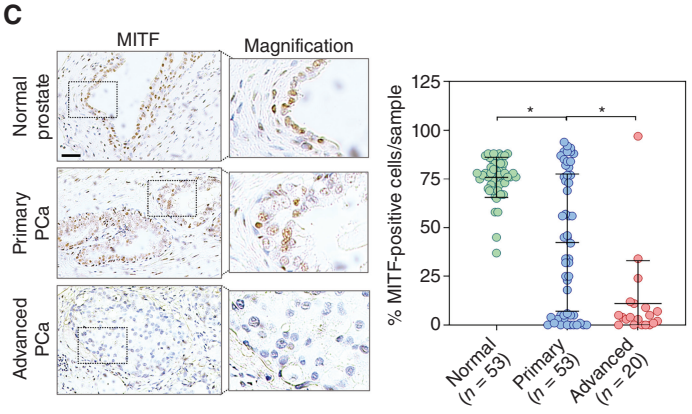

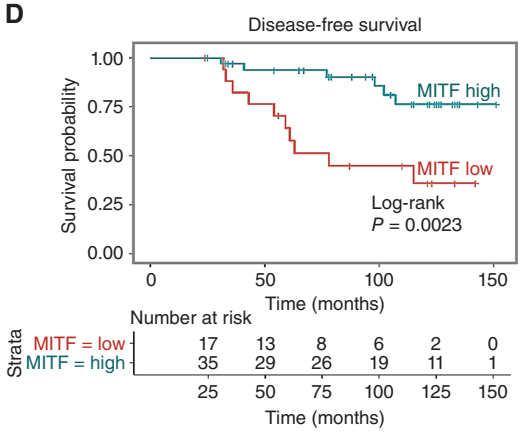

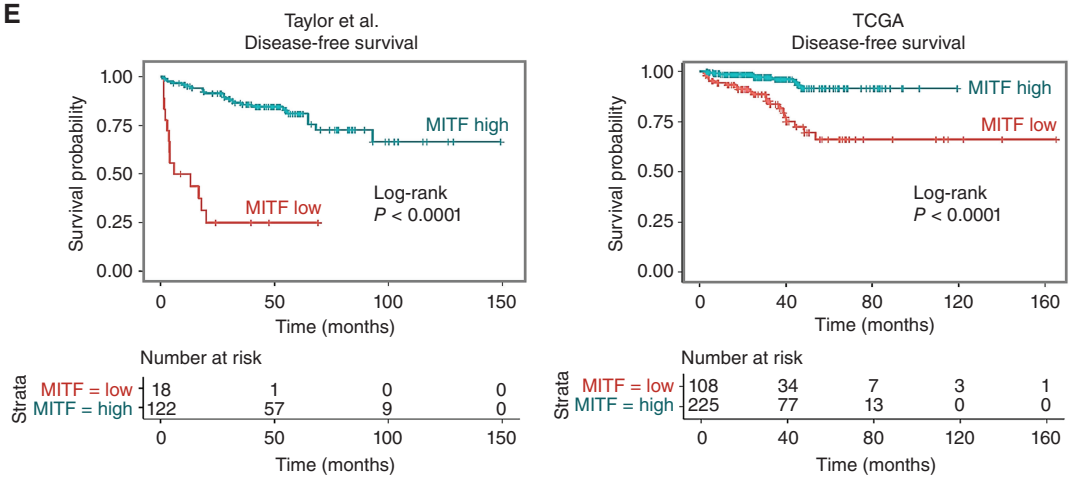

two publicly available datasets with Gleason annotation (Supplementary Fig. S1C). Remarkably, primary tumors displaying a low MITF protein expression showed a higher risk of disease relapse (Fig. 1D). This result was confirmed in the two publicly available gene expression datasets containing primary prostate cancer patient samples with clinical follow-up (Fig. 1E).

To further evaluate the clinical significance of MITF in lethal prostate cancer, we identified the MITF-regulated gene network in prostate cancer, by gene expression profiling and knowledge-based computational studies comparing control and *MITF*-knockdown conditions (Supplementary Fig. S2A) in three prostate cancer cell lines displaying the highest MITF expression (Supplementary Fig. S2B). RNA sequencing followed by differential expression analysis (P_{adj} <0.05) resulted in the identification of a consensus gene signature of MITF-regulated genes (Fig. 2A). Interestingly, gene ontology analysis revealed that the MITF transcriptomic signature was enriched for metabolic-, transport-, and protein-related biological categories (Fig. 2B). Of note, MITF expression and its downstream signature are downregulated in tumor cells when compared with normal cells (Supplementary Fig. S2C) in a publicly available single-cell prostate cancer transcriptomic dataset (45). Further, by gene set enrichment analysis (GSEA), MITF signature was also downregulated in primary prostate cancer samples with a high Gleason score (Supplementary Fig. S2D). Most notably, we observed that advanced metastatic castration-resistant prostate tumors not only expressed lower levels of MITF but also significantly downregulated the MITF gene signature (Fig. 2C). Together, these findings, obtained using multiple publicly available datasets and a cohort of tissue samples, indicate that MITF downregulation may play a key role in the progression of the disease to a lethal metastatic therapy-resistant stage.

Next, we functionally evaluated the *in vivo* aggressiveness of MITF downregulation in prostate cancer cells. We intracardially injected into the left ventricle of mice short hairpin RNA (shRNA) MITF-depleted luciferase-labeled cells (Supplementary Fig. S2E) and observed a significant increase in tumor photon flux (Fig. 2D), which was associated with decreased overall survival (Fig. 2E) when compared with controls. The same results were observed when using CRISPR/Cas9 to knock out the MITFA isoform in 22Rv1 cells (Supplementary Fig. S2F and S2G), the predominant MITF isoform expressed in prostate cancer cell lines (Supplementary Fig. S2H) and in publicly available prostate cancer patient datasets (Supplementary Fig. S2I and S2J). Contrariwise, mice intracardially injected with prostate cancer cells overexpressing MITFA (Supplementary Fig. S2K) showed increased survival (Supplementary Fig. S2L). Thus, these functional studies provide the rationale to further evaluate the mechanisms through which MITF downregulation contributes to the aggressiveness of lethal prostate cancer.

eIF3B Is a Bona Fide MITF-Suppressed Gene That Contributes to Prostate Cancer Aggressiveness

To determine the clinically significant MITF downstream effectors, we selected genes that exhibited common differential expression patterns in both MITF-knockdown prostate cancer cell experimental models and in prostate cancer patient transcriptomic datasets during the progression of primary to lethal prostate cancer, which led to identifying a subset of 11 uniformly deregulated genes (Fig. 3A; Supplementary Fig. S3A). To functionally characterize these genes, we performed a focused loss-of-function genetic screen. After confirming the successful knockdown of the 6 overexpressed target genes in *shMITF* knockdown cells and 5 downregulated target genes in non–MITF-depleted *shControl* cells (Supplementary Fig. S3B and S3C), we monitored the resulting viability of prostate cancer cells. Notably, the knockdown of five genes, *eIF3B* and *RRS1* in the upregulated group and *ATPV0E1*, *TMEM243,* and *FYCO1* in the downregulated group, had a significant impact on colony formation (Fig. 3B and C).

We focused on dissecting the functional interplay between MITF and eIF3B, the MITF-suppressed gene that most strongly affected the viability of prostate cancer cells in our screen (Fig. 3B). We first confirmed that MITF and eIF3B are inversely expressed in clinical prostate cancer tissue samples. Analysis of four publicly available prostate cancer patient datasets revealed a strong inverse correlation at the mRNA level between *MITF* and *eIF3B* (Fig. 3D; Supplementary Fig. S3D). This result was also observed between *MITFA* and *eIF3B* in the two publicly available transcriptomic datasets that discriminate among different *MITF* isoforms (Supplementary Fig. S3E). IHC analysis of prostate cancer tissue samples further demonstrated an inverse association between MITF and eIF3B protein expression (Fig. 3E).

In addition, we functionally evaluated whether *eIF3B* is a direct effector gene of MITF. Indeed, *eIF3B* mRNA (Supplementary Fig. S3F) and protein levels (Supplementary Fig. S3G) increased after MITF depletion, and opposite results were observed when MITFA was overexpressed (Supplementary Fig. S3H and S3I). Notably, confirming that eIF3B mediates the biological properties of MITF, we observed that eIF3B overexpression (Supplementary Fig. S3J) rescued the growth decrease induced by MITFA in prostate cancer cells (Fig. 3F).

Next, we sought to determine the transcription-based mechanism through which MITF represses *eIF3B* expression. Remarkably, MITF chromatin immunoprecipitation-sequencing (ChIP-seq) in 22Rv1 cells identified MITF *eIF3B* promoter occupancy (Fig. 3G). Of note, an unbiased

Figure 2. MITF downregulation increases the aggressiveness of prostate cancer. **A,** Heat map of MITF gene signature in DU145, 22Rv1, and ARCaPM cells transfected with siControl or two siRNAs targeting MITF, in triplicates. Red and blue colors indicate high and low gene expression, respectively. **B,** Biological processes (FDR ≤0.05) identified by gene ontology (GO) analysis of MITF gene signature. **C,** Modulation of MITF target gene signature from **A** in primary and advanced prostate cancer (PCa) patient samples from three publicly available datasets (GSE35988, GSE21032, and GSE3933). Orange and green colors indicate statistical significance (FDR) of induction and suppression of the target gene signatures, respectively (modified GSEA). **D,** Representative image and quantification of photon flux signals of mice intracardially injected with 10^5 DU145, 22Rv1, and ARCaPM shControl (**C**) or shMITF luciferase-tagged cells after 21 days. Ten male mice were used in each experimental group. **E,** Survival curves of mice from **D**. *, $P < 0.05$.

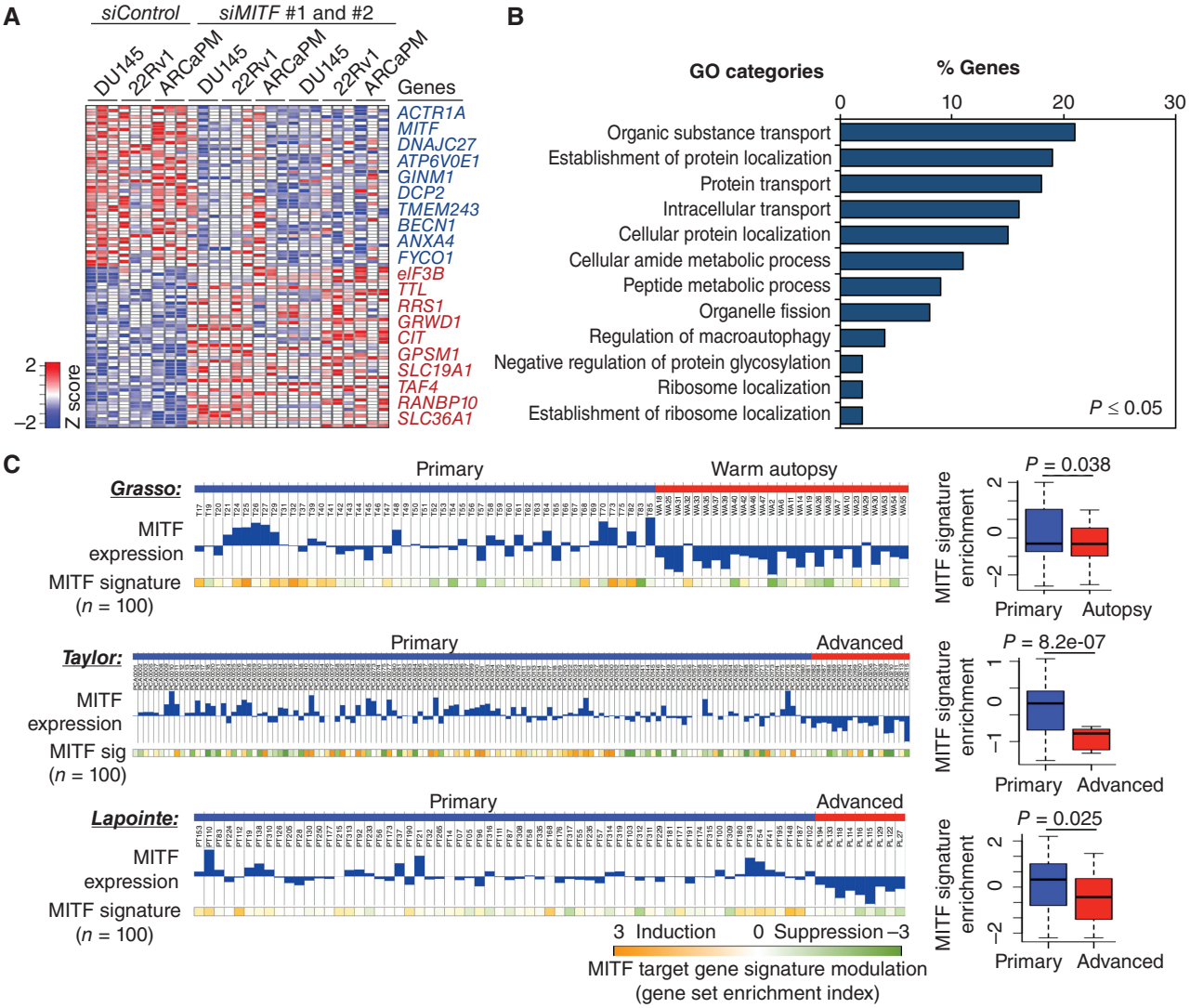

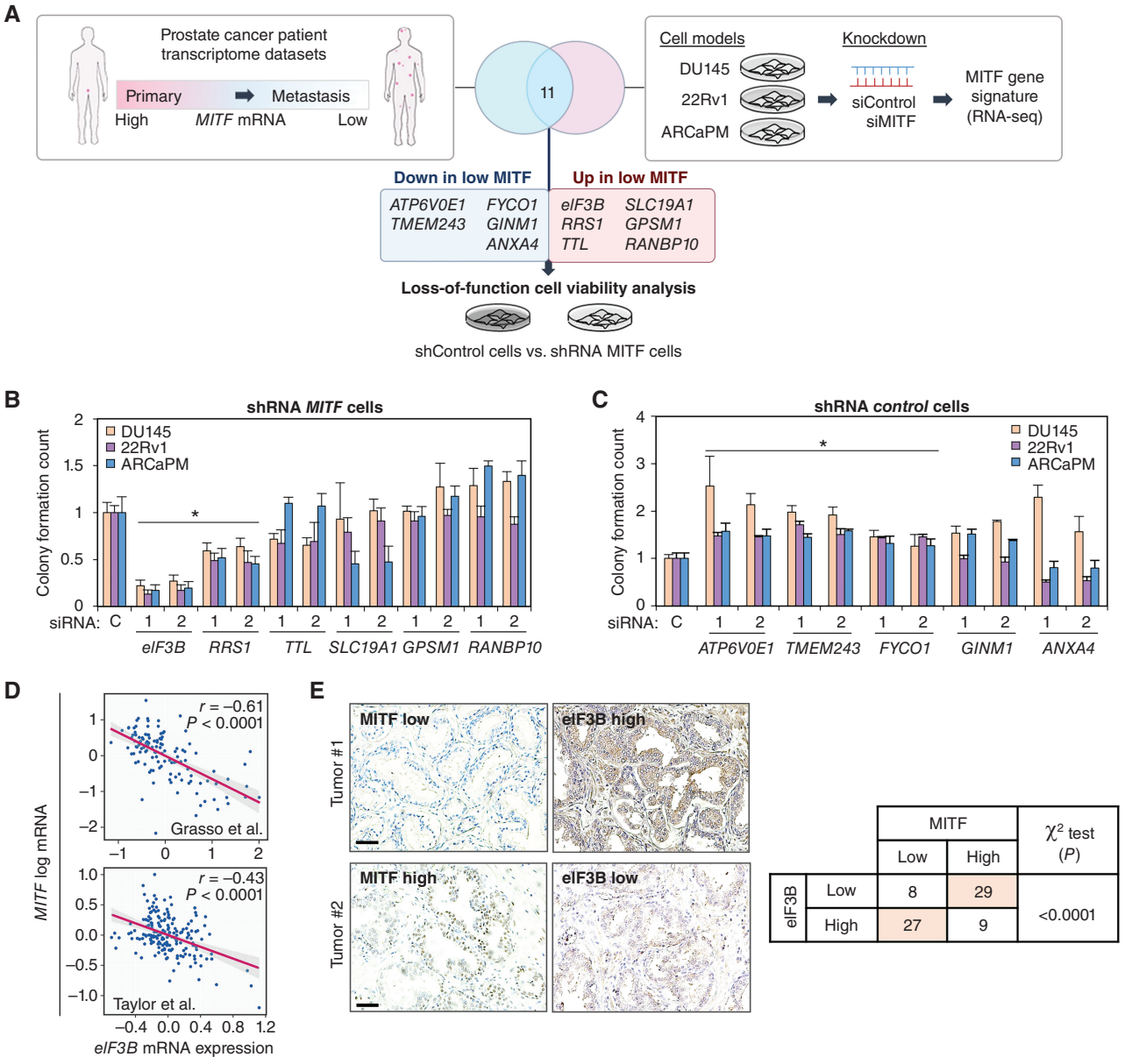

		MITF		χ^2 test (*P*)
		Low	High	
eIF3B	Low	8	29	<0.0001
	High	27	9	

Figure 3. eIF3B is a direct functional effector gene of MITF in prostate cancer. **A,** Diagram illustrates the experimental workflow used to identify and functionally validate 11 commonly deregulated genes in three MITF-depleted experimental models and two publicly available patient datasets (GSE35988 and GSE21032). RNA-seq, RNA sequencing. **B** and **C,** Quantification of colony formation in DU145, 22Rv1, and ARCaPM cells with upregulated (stable shMITF cells; **B**) and downregulated (shControl cells; **C**) target genes transfected with control siRNA or two siRNAs targeting each MITF target gene. C, control. **D,** Pearson correlation analysis between *MITF* and *eIF3B* gene expression levels in indicated publicly available clinical prostate cancer datasets (GSE35988 and GSE21032). **E,** Representative MITF and eIF3B IHC and quantification in prostate cancer tissue samples. The MITF staining was scored as low ≤20% positive nuclei and high >20% positive nuclei, and eIF3B staining intensity was scored as low (– or +) and high (++) in three different areas of each tumor section. χ^2 test = Chi-square test. Scale bar, 100 μm. (*continued on following page*)

analysis of multiple publicly available MITF ChIP-seq data from several cancer types identified consistent MITF prominent peaks in the *eIF3B* promoter (Supplementary Fig. S3K). Indeed, we identified five MITF-binding elements (MBE) that we termed MBE 1 to 5 in the *eIF3B* promoter. ChIP followed by qPCR assays revealed that MITF occupies the five MBEs, but not the adjacent control region, and that a specific promoter region, constituting less than 200nt and containing MBE 2 and 3, showed the highest MITF binding (Fig. 3H). In addition, an *eIF3B*-promoter cotransfection reporter assay showed that MITF depletion activated luciferase transcription (Fig. 3I). On the contrary, overexpression of MITFA repressed transcription and mutation of the MBEs significantly reduced this effect (Fig. 3J), further confirming MITF regulation of *eIF3B* transcription by direct promoter binding. Thus, altogether these data demonstrate that *eIF3B* is a direct downstream MITF-repressed gene.

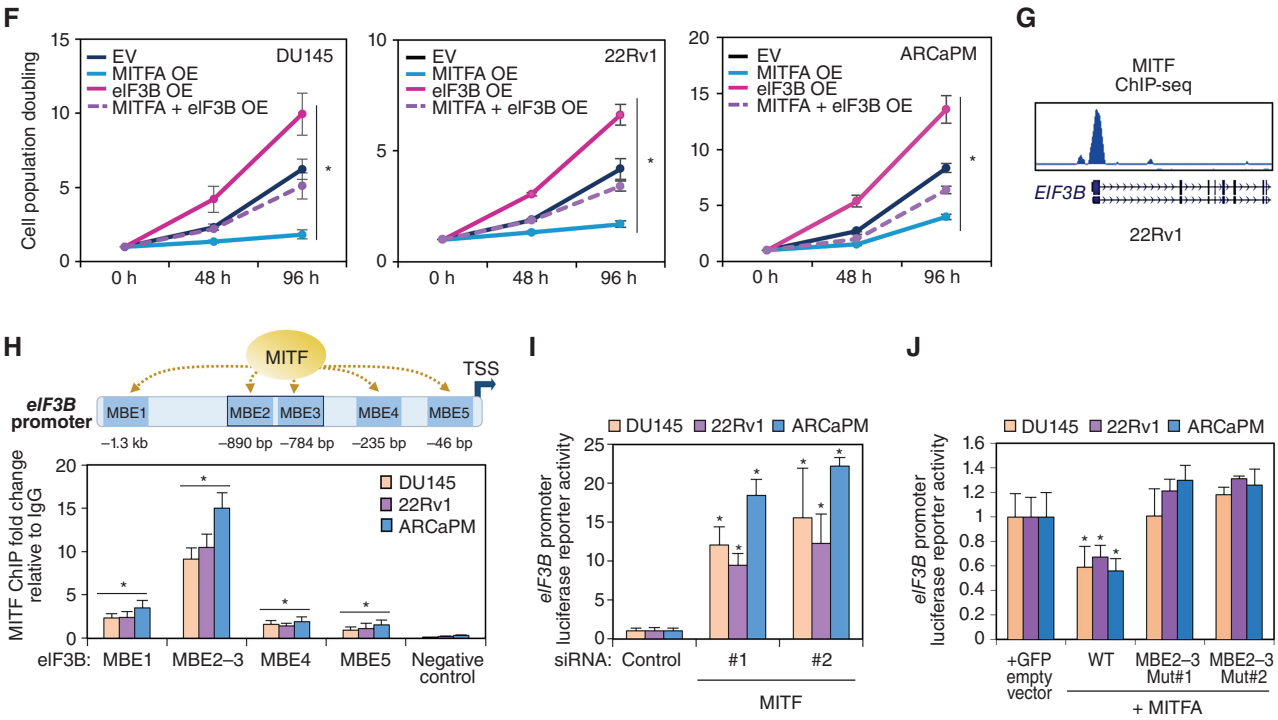

Figure 3. ***(Continued)*** **F,** Quantification of cell population doubling in DU145, 22Rv1, and ARCaPM cells transfected with empty (EV), MITFA, and/or eIF3B vectors. OE, overexpression. **G,** MITF ChIP-sequencing profile at the *eIF3B* locus in 22Rv1 cells. **H,** Cartoon depicting the five predicted MITF-binding elements (MBE) in the promoter region of *eIF3B* and ChIP-qPCR of MITF occupancy at MBE1–5 and flanking negative region in the *eIF3B* promoter of DU145, 22Rv1, and ARCaPM cells. TSS, transcription start site. **I,** Luciferase *eIF3B* promoter activity in DU145, 22Rv1, and ARCaPM cells following cotransfection of siRNA control or two siRNAs targeting MITF, or a Renilla transfection control (normalized relative to control siRNA). **J,** Luciferase *eIF3B* promoter activity in DU145, 22Rv1, and ARCaPM cells following cotransfection with an empty or MITFA vector, *eIF3B* promoter luciferase reporter wild-type (WT) or mutated MBE2–3, or a Renilla transfection control. Data, mean ± SD of at least 3 experiments. *, $P < 0.05$.

The MITF–eIF3B Axis Regulates a Specialized Translation Circuitry Including AR and MHC-I mRNAs

Based on previous studies proposing that the eIF3 complex may promote or repress translation of specific mRNAs (34–36), we next investigated the impact of the MITF–eIF3B axis in regulating translation specificity in prostate cancer. For this purpose, we performed eIF3B enhanced cross-linking immunoprecipitation sequencing (eCLIP-seq) in prostate cancer cells. We observed strong enrichment of signals in the eIF3B eCLIP samples relative to the input, and peak calling analysis identified 15,102 regions with significant eIF3B binding ($\log_2$ fold change ≥3 and $-\log_{10}(P)$ ≥3, $n = 3$; Supplementary Fig. S4A; Supplementary Table S2). These peaks were observed in 6,061 genes with distinct mRNA dysregulation between localized and advanced disease in three publicly available prostate cancer datasets (Supplementary Table S3). eIF3B binding was remarkably represented in the 5′UTRs, covering up 65.4% of the enriched peaks (Fig. 4A). Moreover, Hypergeometric Optimization of Motif EnRichment (HOMER) analysis on the 5′UTR binding sites identified an eight-nucleotide long U and C pyrimidine–rich motif (UC motif) with $P = 1e{-}121$ that appeared in 1,541 peaks (Fig. 4B). Of note, gene ontology (GO) analysis of eIF3-binding peak enriched mRNAs containing the UC-rich 5′UTR motif not only determined biological processes related to ribosome biogenesis and protein processing but also enriched for cellular response to peptide hormone stimulus and immune response (Fig. 4C). Because castration resistance and immune evasion are biological processes of paramount importance in the pathogenesis of lethal prostate cancer, we decided to investigate further these two categories focusing on AR, a key TF driving pathogenesis in all stages of prostate cancer (4, 46) and MHC-I members (HLA-A, -B, and -C), which play a fundamental role in antigen presentation to $CD8^+$ T lymphocytes (47, 48). Importantly, the 5′ UTRs of *AR, HLA-A, -B,* and *-C* contained eIF3B eCLIP-seq peaks with the UC-rich motif (Fig. 4D and E; Supplementary Fig. S4B and S4C). To further evaluate if eIF3B modulates the expression of these molecules at the translational level, we conducted immunoblot and qPCR analysis of empty vector and eIF3B transduced cells. We observed that eIF3B overexpression did not induce a significant increase in other eIF3 subunits (Supplementary Fig. S4D), whereas an increased global protein synthesis measured by puromycin incorporation in nascent peptides was observed (Supplementary Fig. S4E). Surprisingly in this context, AR protein expression increased, and MHC-I levels decreased (Fig. 4F), whereas mRNA levels remained unchanged (Fig. 4G). Of note, AR protein increase induced by eIF3B was not ascribed to an increase in AR protein half-life (Supplementary Fig. S4F). To further assess eIF3B

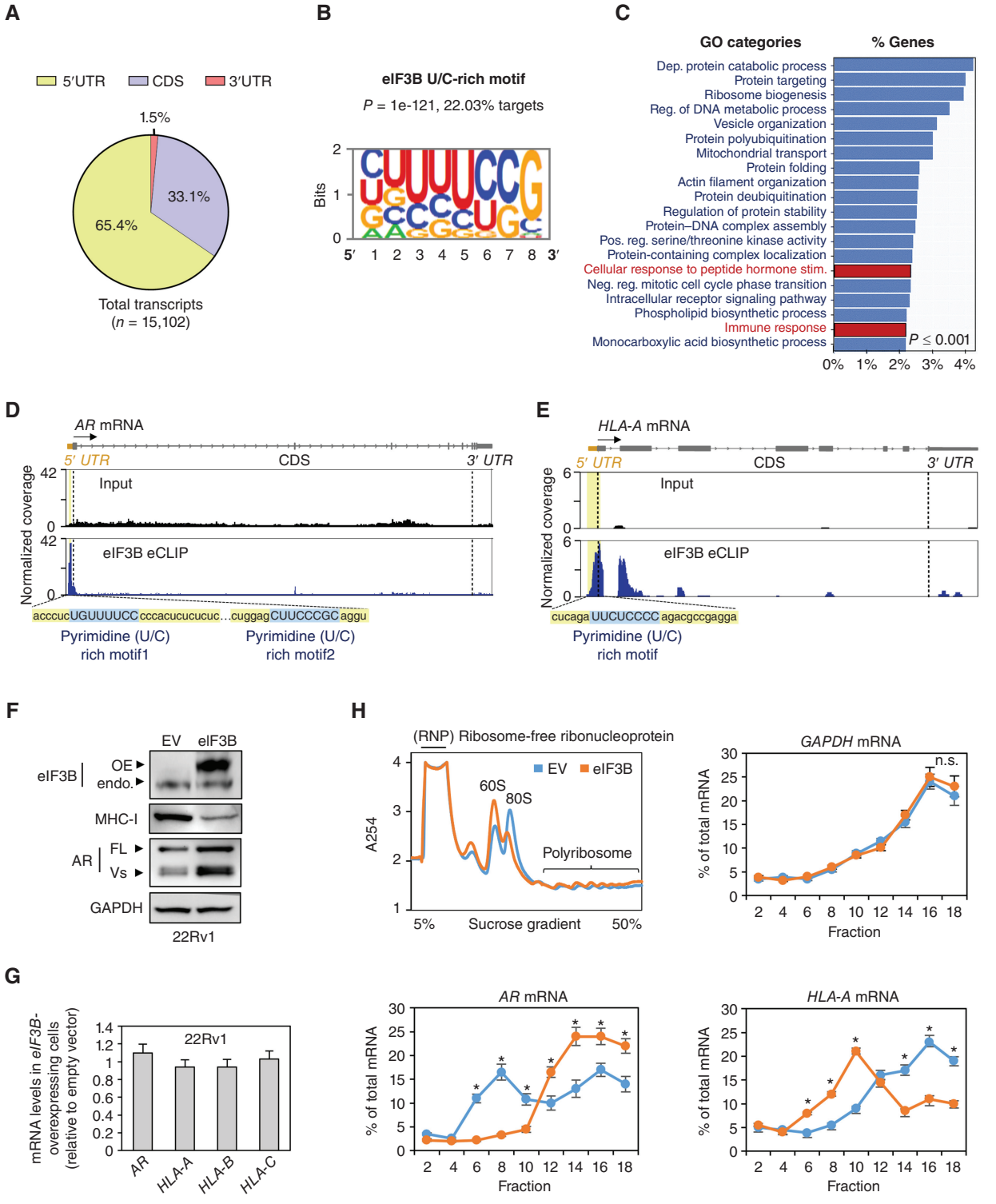

Figure 4. The MITF–eIF3B axis regulates a specialized translation circuitry in prostate cancer. **A,** 5′UTR, coding sequence (CDS), and 3′UTR peak distribution in triplicate eIF3B eCLIP-seq. **B,** HOMER motif analysis of 5′UTR peaks reveals an 8-nucleotide UC motif. **C,** GO biological categories significantly (FDR < 0.01) enriched for transcripts containing the 5′UTR UC motif peaks. Dep., dependent; Neg. reg., negative regulation; Pos. reg., positive regulation; Reg., regulation. **D** and **E,** eIF3B eCLIP and input plots of the *AR* (**D**) or *HLA-A* (**E**) transcript. Blue indicates the UC-rich motifs. **F,** eIF3B, MHC-I, and AR immunoblot in 22Rv1 cells transduced with empty (EV) or eIF3B vector. endo, endogenous; FL, full length; OE, overexpression; Vs, variants. **G,** Quantification of mRNA levels of specified genes in 22Rv1 cells transduced with and EV or eIF3B vector. **H,** Polysome profiling of 22Rv1 cells transduced with EV or eIF3B vector. *AR*, *HLA-A*, and *GAPDH* mRNA levels were determined by qPCR from polysome fractions of 22Rv1 cells transduced with EV or eIF3B vector. Percentage of *AR*, *HLA-A*, and *GAPDH* mRNA distributed in each fraction against total mRNA is shown. (*continued on following page*)

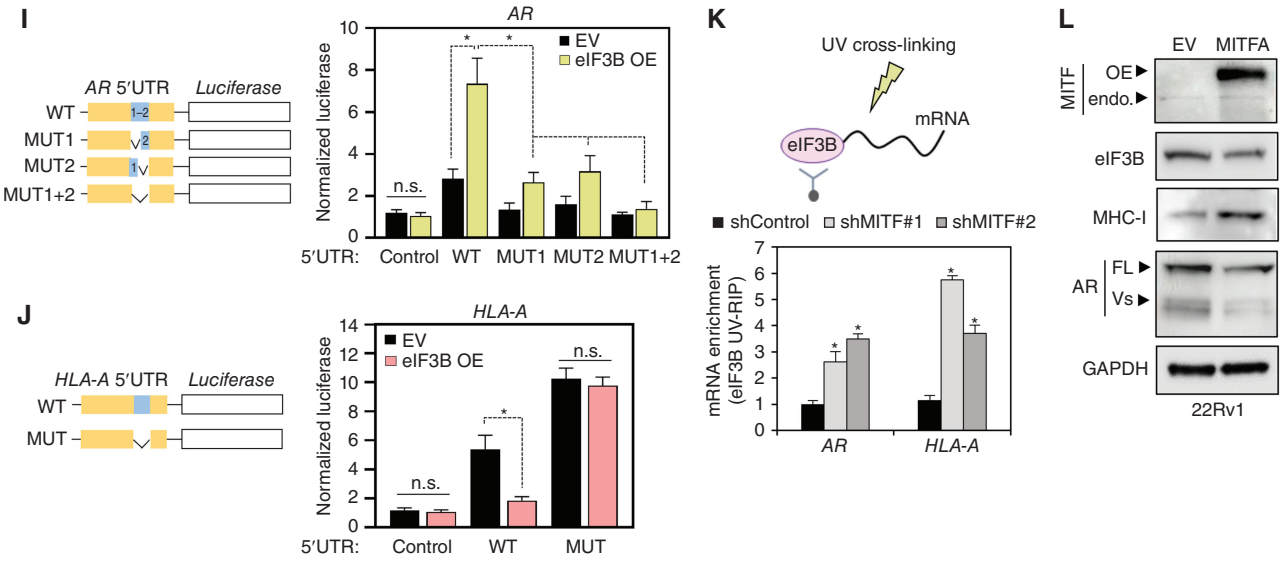

Figure 4. ***(Continued)*** **I** and **J,** WT or HOMER UC motif deletion mutant of *AR* (**I**) or *HLA-A* (**J**) 5′UTRs with Firefly luciferase reporter constructs were transfected, and each luciferase reporter activity measured in 22Rv1 cells transduced with EV or eIF3B vector. Results were normalized to Renilla expression and luciferase mRNA. **K,** *AR* and *HLA-A* mRNA enrichment in eIF3B UV-RIP in shControl or shMITF 22Rv1 cells. **L,** MITF, eIF3B, MHC-I, and AR immunoblot in 22Rv1 cells transduced with an EV or MITFA vector. Data, mean ± SD of at least 3 experiments. n.s., not significant. *, $P < 0.05$.

regulation of AR and HLA-A translation, we performed polysome profiling in empty vector or eIF3B transduced cells. Overexpression of eIF3B resulted in a significant increase in *AR* and reduction in *HLA-A* mRNAs in polysomes, whereas the mRNA of the housekeeping gene *GAPDH* in polysomes did not change (Fig. 4H).

Next, to determine whether eIF3B levels regulate AR and HLA-A expression through the UC-rich 5′UTR motif, we generated luciferase reporter systems that included the 5′UTRs of *AR* or *HLA-A*, containing a wild-type (WT) or a regulatory element deletion mutant. These constructs were subsequently transduced into 22Rv1 control and eIF3B-overexpressing cells, and we observed that WT *AR* 5′UTRs displayed an increase in luciferase activity upon induction of eIF3B overexpression, whereas the opposite was observed in *HLA-A* (Fig. 4I and J). However, the noninsert control vector and the UC-rich motif deletion in *AR* and *HLA-A* 5′UTRs were both insensitive to eIF3B overexpression (Fig. 4I and J). Interestingly, swapping the 5′UTR UC-rich motif from *AR* to *HLA-A* and vice versa did not alter luciferase activity upon induction of eIF3B overexpression (Supplementary Fig. S4G). Thus, suggesting that, although the UC-rich motif is necessary for eIF3B binding to 5′UTRs, additional mechanisms are responsible for activating or repressing the translation of specific mRNAs. Moreover, the addition of m7G cap analogue to 22Rv1 protein extracts inhibited translation of both AR and HLA-A luciferase reporter mRNAs, indicating that eIF3-dependent translation of both mRNAs is cap-dependent (Supplementary Fig. S4H and S4I). These results suggest that eIF3B in prostate cancer may modulate translation in a transcript-specific manner by recognizing a UC-rich motif and mechanistically explain the biological impact of eIF3B overexpression in lethal prostate cancer.

Furthermore, we confirmed that MITF through eIF3B controls AR and HLA-A expression. eIF3B ultraviolet cross-linked RNA immunoprecipitation (UV-RIP) and quantitative polymerase chain reaction (qPCR) of MITF-depleted prostate cancer cells showed enriched *AR* and *HLA-A* (Fig. 4K) mRNA binding to eIF3B, which resulted in the observed increased AR and decreased MHC-I protein levels (Supplementary Fig. S4J), whereas mRNA levels remained unchanged (Supplementary Fig. S4K). Opposite results were observed on AR and MHC-I protein levels in MITFA-overexpressing prostate cancer cells (Fig. 4L).

Finally, conscious that mTOR is a key regulator of translation (23, 30), we next investigated for potential cross-talk with the MITF–eIF3B axis. Treatment of 22Rv1 and LNCaP cells with the mTOR inhibitor, rapamycin, did not affect either MITF or eIF3B expression (Supplementary Fig. S4L). In addition, MITF depletion did not modify the expression of mTOR-modulated translation, as shown by no changes in phospho-p70 S6 kinase and phospho-4E-BP1 expression (Supplementary Fig. S4M). Thus, these results suggest that the MITF–eIF3B axis impacts translation in prostate cancer cells independently from mTOR pathway activity.

The MITF–eIF3B Axis Confers Resistance to ADT

Because AR overexpression is a frequent adaptive trait conferring resistance to ADT (4, 46), we next raised the question of whether the MITF–eIF3B axis could contribute to castration resistance. Supporting the clinical significance of this axis, we observed a strong MITF-negative and eIF3B-positive correlation with an AR effector signature of 31 genes (49) in multiple publicly available prostate cancer patient datasets (refs. 39, 40, 50, 51; Fig. 5A; Supplementary Fig. S5A). Functionally, we observed that

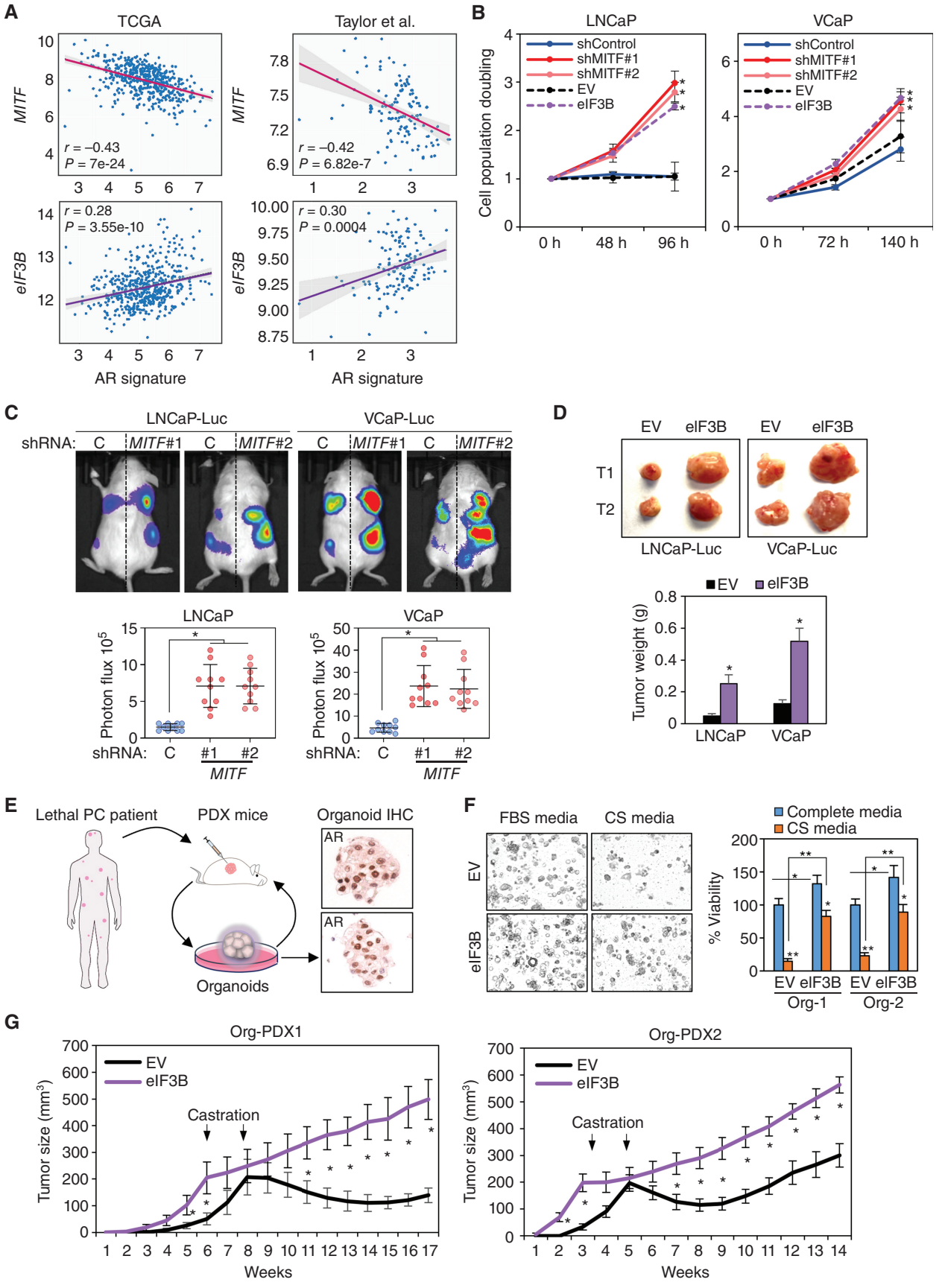

in the androgen-responsive prostate cancer cells, LNCaP and VCaP, MITF depletion increased *eIF3B* mRNA (Supplementary Fig. S5B), as well as eIF3B and AR protein levels (Supplementary Fig. S5C). The increase in AR protein expression under MITF-knockdown conditions also increased the transcription of the AR-regulated genes *KLK3* and *TMPRSS2* (Supplementary Fig. S5D). Opposite results were observed when overexpressing MITFA (Supplementary Fig. S5E and S5F). Notably, both MITF knockdown and eIF3B overexpression increased LNCaP and VCaP proliferation when cultured in charcoal-stripped (CS) serum media (Fig. 5B) and conferred resistance to the antiandrogen receptor antagonist enzalutamide (Supplementary Fig. S5G and S5H). Of note, we observed that when degrading AR protein using the ARV-110 proteolysis-targeting chimera (PROTAC; Supplementary Fig. S5I), eIF3B-overexpressing prostate cancer cell proliferation significantly decreased (Supplementary Fig. S5J), thus further supporting that AR modulation by eIF3B is key in conferring resistance to ADT. Moreover, the proliferation of MITF-knockdown cells was higher than control cells in the presence of 1 nmol dihydrotestosterone (DHT) than when cultured with 10 nmol DHT (Supplementary Fig. S5K). Notably, *in vivo* subcutaneous tumors generated in castrated mice from LNCaP and VCaP *shMITF*- or eIF3B-overexpressing cells grew faster when compared with control tumors, as demonstrated by photon flux (Fig. 5C) and tumor weight (Fig. 5D; Supplementary Fig. S5L).

Furthermore, we investigated if eIF3B overexpression contributes to castration resistance in patient-derived models (Fig. 5E). Indeed, consistent with the above results, eIF3B overexpression in hormone-sensitive organoids generated from patient-derived prostate cancer xenograft models (44, 52) increased AR protein levels (Supplementary Fig. S5M) without affecting mRNA levels (Supplementary Fig. S5N), and significantly increased organoid viability when cultured in CS serum media (Fig. 5F). Remarkably, *in vivo* subcutaneous tumors generated from eIF3B-overexpressing organoids grew faster in intact and castrated mice than in tumors derived from isogenic empty vector control organoids (Fig. 5G).

Collectively, these results from cell line and patient-derived models indicate that the MITF–eIF3B axis by modulating AR protein expression may contribute to prostate cancer progression to antiandrogen therapy.

The MITF–eIF3B Axis Promotes Immune Evasion

Mechanisms of immune evasion are multifactorial (53) and include major histocompatibility complex class I (MHC-I) downregulation (54–60). Given that the MITF–eIF3B axis curtails MHC-I expression, we next raised the question if the identified signaling axis contributes to immune evasion in prostate cancer. Supporting the clinical relevance of this axis, we observed in patient tumor samples that high eIF3B protein expression was significantly associated with a lower MHC class I protein abundance (Fig. 6A) and a lower tumor-infiltrating lymphocyte CD8/CD3 ratio (Fig. 6B). In addition, interrogation of prostate cancer tissue samples from multiple publicly available primary and metastatic therapy-refractory patient transcriptomic datasets (39, 40, 50, 51, 60) showed *eIF3B* mRNA levels to be negatively correlated with a T effector mRNA signature (Fig. 6C), whereas no significant association was identified between *eIF3B* mRNA levels and an *MHC-I* mRNA signature (Supplementary Fig. S6A), thus pointing to a translation-based eIF3B–MHC-I immune evasion mechanism.

To determine whether the MITF–eIF3B axis inhibits anticancer immune responses, we assessed this axis in TRAMP-C2 and MyC-CaP mouse cell lines and observed that both MITF depletion (Supplementary Fig. S6B) or eIF3B overexpression (Supplementary Fig. S6C) decreased MHC-I protein expression, without affecting the mRNA levels (Supplementary Fig. S6D and S6E). To test the impact of this signaling axis on immune evasion, we injected eIF3B-overexpressing and empty vector TRAMP-C2 and MyC-CaP cells subcutaneously into C57BL/6 and FVB/N male mice, respectively. Once tumors formed, Poly(I:C) was intratumorally injected to trigger an immune response (61, 62). Poly(I:C) administration decreased the growth of control (TRAMP-C2 and MyC-CaP empty vector) tumors (Fig. 6D) and prolonged the overall mouse survival (Supplementary Fig. S6F). Notably, the growth-inhibiting effect of Poly(I:C) disappeared in eIF3B-overexpressing tumors (Fig. 6D; Supplementary Fig. S6F). Moreover, we observed that eIF3B-overexpressing tumors treated with Poly(I:C) had significantly lower cytotoxic $CD8^+$ T-infiltrating cells, including cytotoxic granzyme B–positive $CD8^+$ T cells (Fig. 6E and F; Supplementary Fig. S6G) when compared with control tumors. To further determine the contribution of T-cell surveillance on eIF3B-dependent tumor growth, we subcutaneously injected empty vector (control) and eIF3B-overexpressing cells into immunocompetent (C57BL/6 and FVB/N) or immunocompromised (NOD/SCID) mice that lack functional T cells. Notably, we observed that the lack of T cells in NOD/SCID mice decreased the differences in tumor growth between control and eIF3B-overexpressing tumors (Supplementary Fig. S6H). Next, we investigated if the MITF–eIF3B axis could confer resistance to

Figure 5. The MITF–eIF3B axis confers resistance to ADT. **A,** Pearson correlation analysis between *MITF* or *eIF3B* mRNA abundance with the expression of a 31-androgen receptor signature in tumor specimens from the indicated prostate cancer datasets (https://www.cancer.gov/tcga and GSE21032). TCGA, The Cancer Genome Atlas. **B,** Cell population doubling of LNCaP and VCaP cells transduced with shControl, shMITF, empty (EV), or eIF3B vector cultured in CS FBS and phenol red–free media. **C,** Representative imaging and quantification of tumor photon flux signals in castrated mice after 6 weeks of subcutaneous injection of 10^6 LNCaP and VCaP shControl or shMITF luciferase-tagged cells. Ten mice were used for each experimental group. C, control. **D,** Representative image and quantification of tumor weights in castrated mice subcutaneously injected with 10^6 LNCaP and VCaP EV or eIF3B vector luciferase-tagged cells. **E,** Diagram depicts the workflow used to generate patient-derived hormone-sensitive xenograft and organoid models. PC, prostate cancer; PDX, patient-derived xenograft. **F,** Representative image and cell viability (MTS) quantification of EV or eIF3B-overexpressing prostate cancer organoids cultured in regular media supplemented with FBS 10% or CS and phenol red–free media. **G,** Tumor growth curves of subcutaneous tumors generated after injecting control (EV) or eIF3B-overexpressing organoids (Org) in intact host mice and after castration. Mice were castrated (arrow) once tumors reached a size of 200 mm^3. Ten mice were used for each experimental group. Data, mean ± SD of at least 3 experiments. *, $P < 0.05$; **, $P < 0.0001$.

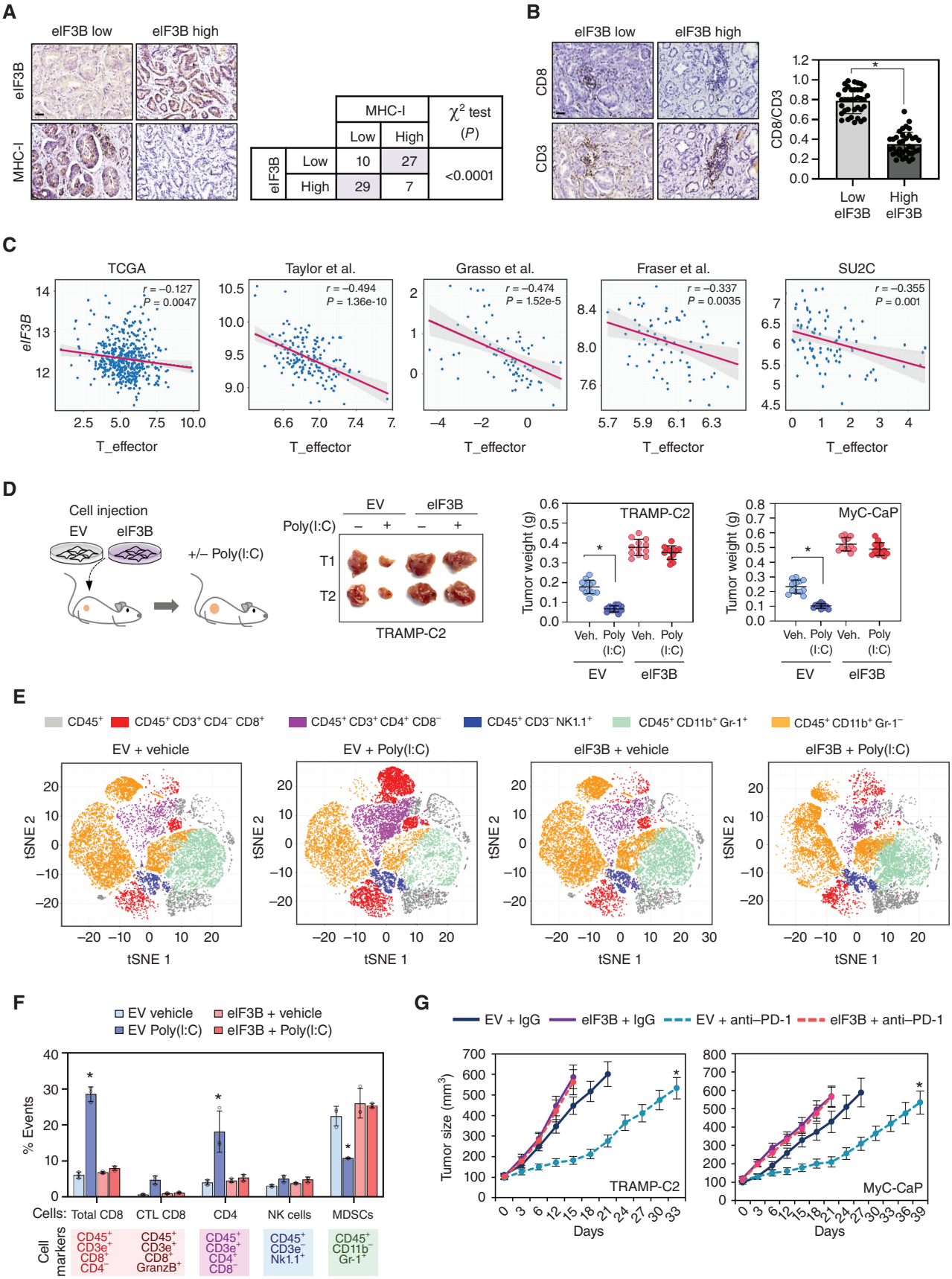

		MHC-I		χ^2 test (*P*)
		Low	High	
eIF3B	Low	10	27	<0.0001
	High	29	7	

immune-checkpoint inhibitor (ICI) therapy. Similar to what we observed with Poly(I:C), eIF3B overexpression not only reduced the therapeutic efficacy of anti–PD-1 (Fig. 6G) but also decreased the accumulation of CD8$^+$ T cells in TRAMP-C2 and MyC-CaP tumors (Supplementary Fig. S6I and S6J). Of note, the immune evasion effects induced by eIF3B overexpression were not ascribed to changes in eIF4E and eIF4G levels or subunit complex assembly (Supplementary Fig. S6K).

These data support that eIF3B elevation inhibits T-cell–mediated immune response and may contribute to the observed limited clinical efficacy of immune-checkpoint inhibitors in lethal prostate cancer.

Targeting the MITF–eIF3B Axis Enhances Androgen Deprivation and Immune-Checkpoint Therapy Efficacy

Given that eIF3B increase upon MITF downregulation in prostate cancer modulates the expression of key molecules associated with drug resistance, we investigated whether this axis could be pharmacologically targeted to enhance therapy efficacy.

Proximity ligation (Fig. 7A) and immunoprecipitation (Supplementary Fig. S7A) assays showed that 4EGI-1, a small molecule that disrupts the eIF4E/eIF4G complex translation initiation assembly (63), also impedes eIF3B binding to the translation initiation complex. Indeed, suggesting that eIF3B-dependent translation can be pharmacologically targeted, we observed that 4EGI-1 altered AR and HLA-A translation, whereas GAPDH translation remained unaltered (Fig. 7B) and reverted both the protein increase of AR and decrease in MHC-I induced by eIF3B overexpression in 22Rv1 cells (Fig. 7C) without modifying mRNA levels (Supplementary Fig. S7B). Importantly, these effects were observed at 4EGI-1 concentrations that do not completely inhibit translation, as measured by labeling neonascent peptides with puromycin (Fig. 7D). Notably, supporting that 4EGI-1 impairs eIF3B translation, changes in AR and MHC-I expression induced by 4EGI-1 were also observed when overexpressing the eIF4 translation inhibitor 4E-BP1 (Supplementary Fig. S7C). Remarkably, *in vivo* studies confirmed that 4EGI-1 administration to mice bearing 22Rv1 xenografts disrupted eIF4E–eIF3B complex binding (Supplementary Fig. S7D) and deregulated AR and HLA-A mRNA translation (Supplementary Fig. S7E), resulting in a decreased AR and increased MHC-I protein expression (Supplementary Fig. S7F), without completely abrogating translation (Supplementary Fig. S7G).

Based on recent studies that demonstrated that combined therapies targeting AR in the context of hormone-sensitive disease significantly improved the survival of prostate cancer patients by delaying the onset of castration resistance (64–66), we tested the efficacy of combining 4EGI-1 with ADT. Indeed, as observed with 22Rv1 cells, exposure of hormone-sensitive LNCaP and VCaP cells to 4EGI-1 significantly reduced AR protein levels (Supplementary Fig. S7H) and induced apoptosis of prostate cancer cells cultured in CS serum media (Supplementary Fig. S7I). This result was also observed *in vivo*, where 4EGI-1 in combination with ADT significantly decreased tumor size (Fig. 7E and F) and induced cleaved-caspase 3 expression in LNCaP and VCaP xenografts (Fig. 7G). Moreover, we further tested the efficacy of combining 4EGI-1 with ADT in 3 hormone-sensitive patient-derived xenograft (PDX) models (52). 4EGI-1 administration decreased AR protein expression (Supplementary Fig. S7J) in all three models. Notably, the survival of mice intracardially injected with prostate cancer cells significantly increased when combining 4EGI-1 with ADT compared with each treatment alone (Fig. 7H).

We next investigated if disrupting eIF3B-dependent translation may sensitize prostate cancer cells to immune-checkpoint inhibition. At first, we tested the effect of 4EGI-1 on MHC-I expression in TRAMP-C2 and MyC-CaP mouse prostate cancer cells. Notably, 4EGI-1 resulted in a significant increase in MHC-I protein abundance (Supplementary Fig. S7K), but not mRNA expression (Supplementary Fig. S7L). We further observed that eIF3B-overexpressing cells when exposed to 4EGI-1 increased MHC-I expression (Supplementary Fig. S7M), suggesting that MHC-I decrease induced by eIF3B can be pharmacologically reverted.

Next, we assessed whether 4EGI-1 could increase the efficacy of anti–PD-1 therapy. Notably, *in vivo* 4EGI-1 administration increased MHC-I protein expression (Supplementary Fig. S7N) and significantly potentiated the efficacy of anti–PD-1 therapy, as assessed by decreased tumor growth (Fig. 7I), enhanced tumor infiltration by cytotoxic CD8$^+$ T cells (Supplementary Fig. S7O) and increase in mouse survival (Fig. 7J) when compared with control and single-agent-treated mice. Of note, the effect of combining 4EGI-1 and anti–PD-1 therapy was reverted upon CD8$^+$ T-cell depletion (Supplementary Fig. S7P). Moreover, we observed that the efficacy of combining 4EGI-1 and

Figure 6. The MITF–eIF3B axis promotes immune evasion. **A,** Representative IHC and quantification of eIF3B and MHC-I expression in prostate cancer tissue samples. The eIF3B and MHC-I staining intensity was scored as low (– or +) and high (++) in three different areas of each tumor section. χ^2 test = Chi-square test. **B,** Representative IHC and quantification of the CD8/CD3 ratio in eIF3B low and high expressing prostate tumors. CD8- and CD3-positive cells were counted in three different areas of each tumor section. **C,** Pearson correlation analysis between *eIF3B* mRNA abundance and the expression of a T-cell effector signature (*CD8A*, *GZMA*, and *GZMB*) in tumor specimens from the indicated prostate cancer datasets (https://www.cancer.gov/tcga, GSE21032, GSE84043, and GSE35988, https://github.com/cBioPortal/datahub/tree/master/public/prad_su2c_2019). TCGA, The Cancer Genome Atlas. **D,** Representative image and quantification of tumor weights of empty vector (EV) and eIF3B-overexpressing TRAMP-C2 and MyC-CaP tumors intratumorally injected with vehicle (Veh.; PBS) or Poly(I:C) 2.5 mg/kg, intratumoral. Five male mice were used for each experimental group. **E,** Cytometry by time of flight (CyTOF) analysis of TRAMP-C2 tumors. PhenoGraph-defined cellular distribution and clustering, as defined by tSNE1 and tSNE2 (t-distributed stochastic neighbor embedding), colored by cellular phenotypes in TRAMP-C2 EV and eIF3B-overexpressing tumors from mice at 2 days after the last intratumoral injection of vehicle (PBS) or Poly(I:C). **F,** CyTOF analysis of TRAMP-C2 tumors. Data derived from normalized viable single cells analyzed by the PhenoGraph algorithm are shown in the bar graph as means ± SD ($n = 3$). Statistical significance was determined by one-way ANOVA with Bonferroni correction for multiple tests. CTL, cytotoxic T lymphocyte; MDSC, myeloid-derived suppressor cells; NK, natural killer cells. **G,** Tumor growth curves of TRAMP-C2 and MyC-CaP subcutaneous tumors generated after injecting 10^6 eIF3B-overexpressing or EV cells in mice intraperitoneally treated with IgG or anti–PD-1 (250 μg/i.p., alternate days). Ten male mice were used for each experimental group. Data, mean ± SD of at least 3 experiments. *, $P < 0.05$. Scale bar, 100 μm.

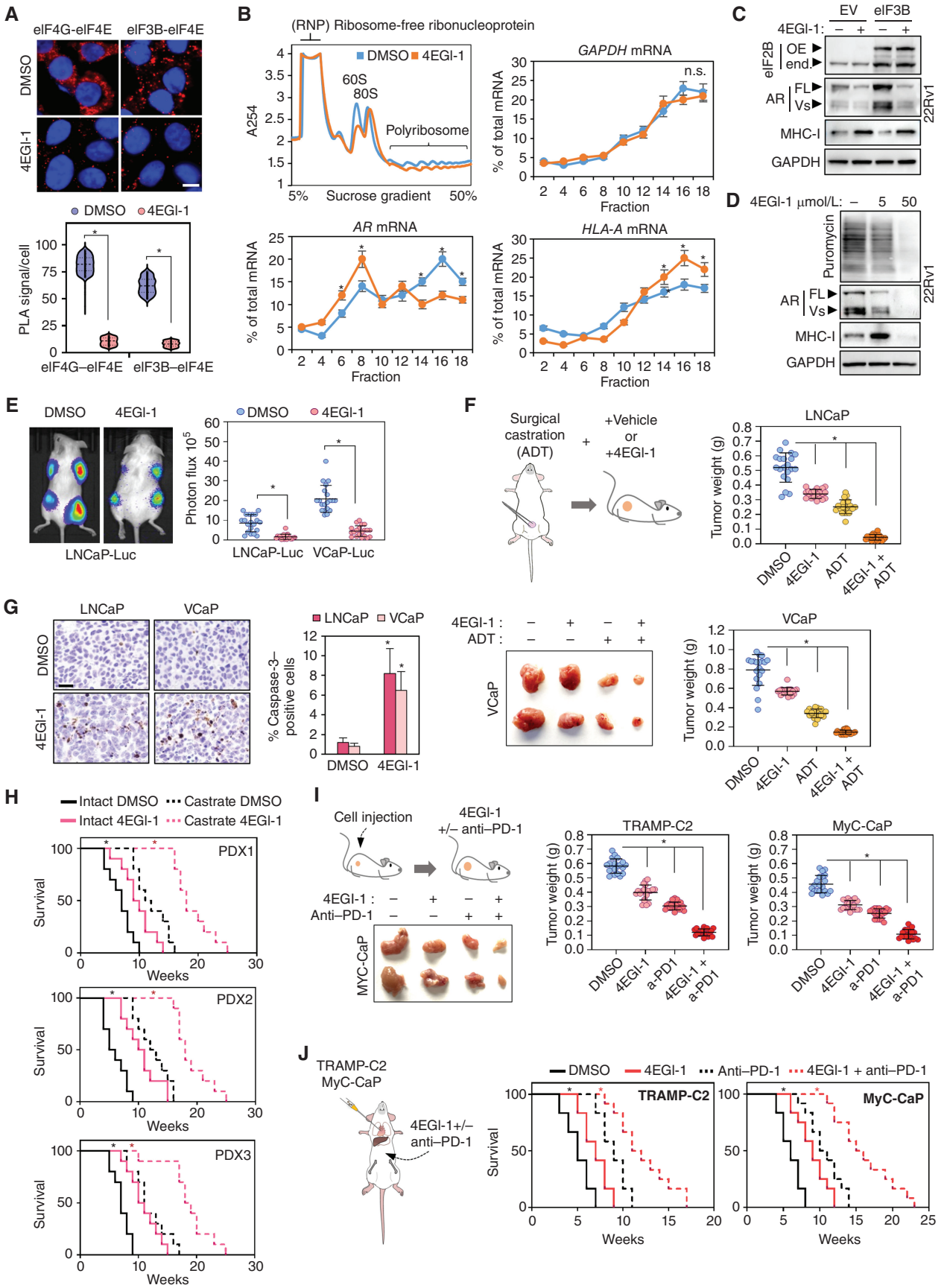

anti–PD-1 decreased in tumors generated from TRAMP-C2 H2-K1/H2-D1 knockout cells (Supplementary Fig. S7Q), indicating that MHC-I expression is necessary to enhance anti–PD-1 efficacy by 4EGI-1.

Altogether, these data demonstrate an eIF3B-dependent translation mechanism that confers therapy resistance and when targeted may increase ADT and ICI efficacy in prostate cancer.

DISCUSSION

The progression of prostate cancer toward a lethal therapy-refractory state is paralleled by a rewiring process in which cancer cells deregulate their signaling programs to survive multiple environmental changes and sustain tumor growth. In this study, we have uncovered that MITF downregulation in prostate cancer transcends beyond its potential tumor-suppressive role in prostate cancer initiation (19) and contributes to key biological properties enabling lethality in prostate cancer patients, namely, castration resistance and decreased immune surveillance, by facilitating eIF3B-dependent translation of specific mRNAs.

By interrogating the expression of master regulator TFs in multiple transcriptome patient datasets, we identified that MITF is consistently downregulated in advanced therapy-refractory prostate cancer samples when compared with primary tumors. Indeed, supporting that MITF downregulation may contribute to the pathogenesis of lethal prostate cancer we observed that MITF expression is most significantly downregulated in advanced therapy-refractory lethal stages of the disease and that primary prostate cancer displaying low MITF levels are significantly associated with disease relapse. These clinical correlates were further validated functionally *in vivo*, where intracardiac injection of MITF-depleted prostate cancer cells decreased the survival of mice. Of note, this observation was confirmed by our converse finding that overexpression of MITFA, the predominant MITF isoform expressed in prostate cancer, significantly reduced prostate cancer aggressiveness. We also show that the role of MITF in prostate cancer is driven by direct promoter binding and subsequent transcriptional regulation of eIF3B, a key component of the translation initiation complex with previously reported oncogenic functions (67).

A critical feature of translational regulation is the ability to promptly rewire the cell proteome in response to changing environments, such as therapy exposure. Translational regulation may modify the signaling activity of specific mRNAs that contribute to cancer cell survival. In this context, we reveal that eIF3B controls the translation of AR and MHC-I. eIF3B eCLIP-seq analysis showed unanticipated specificity of eIF3B binding to a 5′UTR UC-rich motif, and that through this motif binding *AR* and *HLA-A* mRNA translation is dependent on eIF3B amount. These results are in line with previous studies demonstrating specialized mRNA translation by specific eIF3 subunits, which utilizes different modes, including direct interaction with 5′UTR motifs and secondary stem-loop binding, to exert either translational activation or repression (34–36). Indeed, within the context of *AR* and *HLA-A* target mRNAs, the 5′UTR UC-rich motif is required for eIF3B to regulate their translation. However, it remains unresolved how, besides the 5′UTR UC-rich motif, secondary mRNA structure and direct or indirect interaction with RNA binding proteins may either promote or repress the translation of these eIF3B targets. Future studies are required to biochemically address the additional mechanisms that dictate eIF3B translational regulation on specific mRNAs. In addition, our observation that eIF3B participates in cap-dependent translation of AR and MHC-I is consistent with previous publications demonstrating that eIF3 subunits can utilize eIF4E-independent mechanisms of cap-dependent mRNA translation (37, 68).

Advanced prostate cancer unequivocally acquires resistance to ADT and can survive despite low levels of circulating androgens (69). To date, classic mechanisms that underlie the development of ADT resistance include AR overexpression through gene mutations or amplification, changes in androgen biosynthesis, generation of constitutively active AR splice variants, increased AR enhancer activity, and cross-talk with other signaling pathways (70–72). Here we present evidence of a translation mechanism contributing to lethal prostate cancer progression, as we describe how the MITF–eIF3B signaling axis regulates AR protein expression. It is likely that in this context, the MITF–eIF3B axis confers upon prostate cancer cells a rapid increase in AR expression through direct translation regulation, facilitating a timely response to the drastic decrease of circulating androgens induced by ADT.

Translation deregulation by the MITF–eIF3B axis extends beyond AR overexpression and entails pathways that may

Figure 7. Targeting eIF3B-dependent translation increases the efficacy of ADT and ICI therapy. **A,** Representative images and quantification of eIF4G–eIF4E and eIF3B–eIF4E proximity ligation assays (PLA) in 22Rv1 cells treated with vehicle (DMSO) or 4EGI-1 (10 μmol/L) for 24 hours. **B,** Representative polysome profiling; *AR*, *HLA-A*, and *GAPDH* mRNA levels determined by qPCR from polysome fractions of 22Rv1 cells treated with vehicle (DMSO) or 4EGI-1 (5 μmol/L, 24 hours). The percentage of *AR*, *HLA-A*, and *GAPDH* mRNA distributed in each fraction against total mRNA is shown. **C,** eIF3B, AR, and MHC-I immunoblot in 22Rv1 empty vector (EV) or eIF3B-overexpressing cells treated with vehicle (DMSO) or 4EGI-1 (5 μmol/L, 24 hours). endo, endogenous; FL, full length; OE, overexpression; Vs, variants. **D,** Puromycin, AR, and MHC-I immunoblot in 22Rv1 cells cultured with puromycin (100 nmol/L) and treated with vehicle (DMSO) or 4EGI-1 (5 or 50 μmol/L) for 24 hours. **E,** Representative image and quantification of tumor photon flux signals of castrated male mice bearing subcutaneous LNCaP and VCaP luciferase-tagged tumors treated with vehicle (DMSO) or 4EGI-1 (75 mg/kg/i.p., 5 days a week). Five male mice were used for each treatment group. **F,** Experimental diagram and quantification of LNCaP and VCaP tumor weights of intact and castrated (ADT) mice treated with vehicle (DMSO) or 4EGI-1 (75 mg/kg/i.p., 5 days a week) for 28 days. Five male mice were used for each treatment group. **G,** Representative cleaved-caspase 3 IHC and quantification in LNCaP and VCaP xenografts from castrated mice treated with vehicle (DMSO) or 4EGI-1 (75 mg/kg/i.p., 5 days a week) for 1 week. Five male mice were used for each treatment group. **H,** Survival of intact and castrated mice intracardially injected with 10^5 PDX prostate cancer cells treated with vehicle (DMSO) or 4EGI-1 (75 mg/kg/i.p., 5 days a week). *, $P < 0.05$ (intact mice). *, $P < 0.05$ (castrated mice). Ten male mice were used for each treatment group. **I,** Representative image and quantification of TRAMP-C2 and MyC-CaP tumor weight of mice treated with vehicle (DMSO), 4EGI-1 (75 mg/kg/i.p., 5 days a week), anti–PD-1 (250 μg/i.p., alternate days) alone or in combination. Ten male mice were used for each treatment group. **J,** Survival curves of mice intracardially injected with 10^5 TRAMP-C2 and MyC-CaP cells treated with vehicle (DMSO), 4EGI-1 (75 mg/kg/i.p., 5 days a week), or anti–PD-1 (250 μg/i.p., alternate days) alone or in combination. Ten male mice were used for each treatment group. Data, mean ± SD of at least 3 experiments. ns, not significant. *, $P < 0.05$. Scale bar, 100 μm.

be involved in immune evasion, as evidenced by our finding that eIF3B overexpression contributes to MHC-I protein downregulation. Prostate cancer exhibits limited responses to immune-checkpoint blockade therapy (73). Mechanisms associated with this lack of responsiveness are multiple and involve a myriad of signaling pathways, including distinct translational mechanisms that have been mainly focused on studying PD-L1 expression (74–76). Here we demonstrate a novel mechanism by which eIF3B selectively represses *MHC-I* mRNA translation and contributes to the decreased immunosurveillance observed in lethal prostate cancer. Of note, the immunomodulatory eIF3B-dependent translation mechanism identified in our study may cooperate with AR-induced cell-extrinsic and -intrinsic immune evasion (77–80), as well as contribute to immune evasion in the absence of AR expression in prostate cancer. Indeed, the immunoregulatory role of the MITF–eIF3B axis may transcend beyond prostate cancer, because MITF binds to the eIF3B promoter in multiple cancer cell types (see Supplementary Fig. S3K). Thus, for example, low MITF expression in melanoma cells may confer resistance to immunotherapy (81) by not only inducing dedifferentiation and lack of antigen production (82), but also by decreasing antigen presentation through eIF3B-mediated MHC-I translation repression.

The biological pathways influenced by the MITF–eIF3B axis are therapeutically relevant. Indeed, our results demonstrate that pharmacologic targeting of translation subunits does not exclusively decrease general translation, but may also remodel the translatome, as previously demonstrated by others (83). Here we show that the small-molecule 4EGI-1, designed to disrupt the interaction between translation initiation factors, can also modulate the eIF3B-dependent translation of AR and MHC-I. Remarkably, 4EGI-1 not only disrupted eIF3B binding to eIF4 but also modulated AR and MHC-I expression in prostate cancer cells overexpressing 4E-BP1. Consequently, we observed that exposure of prostate tumors to 4EGI-1 at concentrations that do not completely block translation decreased AR and increased MHC-I expression, enhancing the efficacy of ADT and anti–PD-1 therapy. Thus, our results provide proof of concept on how disrupting eIF3B-dependent translation may lead to novel therapeutic strategies and strongly advocate for the need to further develop more potent and specific eIF3 inhibitors.

In summary, this study uncovers how the MITF–eIF3B axis contributes to the pathobiology of lethal prostate cancer and broadens our understanding of how the cancer cell rewires distinct signaling pathways coupling transcription and translation mechanisms that provide the rationale to develop more effective therapeutic strategies.

METHODS

Human Prostate Cancer Tissues

Anonymized human formalin-fixed, paraffin-embedded (FFPE) primary (n = 53) and advanced metastatic castration-resistant prostate cancer (n = 20) tissue samples were collected from the Mount Sinai GU Biorepository (IRB#11-01565) under Institutional Review Board–approved protocol. All patients provided written informed consent to obtain tumor biopsies. All tissue sections were reviewed by a pathologist to confirm prostate cancer origin.

Animal Experimental Models

All animal experiments were performed in the AAALAC-accredited Comparative Bioscience Center at Mayo Clinic. Experiments were in accordance with NIH guidelines for animal care and use, and approved and overseen by the Mayo Clinic Institutional Animal Care and Use Committee. All mouse procedures were performed with immunocompromised (CB17-Prkdcscid/; RRID:IMSR_JAX:001303) and immunocompetent (FVB/N; RRID:IMSR_JAX:001800 and C57BL/6; RRID:IMSR_JAX:005304) obtained from The Jackson Laboratory. For castration, anesthetized and surgically prepared animals were placed in dorsal recumbency. Both testes were then pushed down into the scrotal sacs by pressuring the abdomen. A 1-cm incision was made in the scrotum to expose the tunica. The tunica was pierced, and the testes were pushed out one at a time and then raised to expose the underlying blood vessels. The vas deferens with the prominent blood vessels running along them were located using a forceps and the testis were dissected away from the fat and removed. The vas deferens and ducts were then replaced back into the tunica, and skin incisions were closed with stainless steel wound closures and removed after 10 days. For intracardiac injections, 3- to 4-week-old mice were used. For the rest of the experiments 6- to 7-week-old mice were used. See Methods for mouse work-specific procedures.

Prostate Cancer Cell Lines, Syngenic Mouse Tumors, and Preclinical Patient-Derived Xenograft and Organoid Models

The authenticated prostate cancer DU145 (RRID:CVCL_0105), 22Rv1 (RRID:CVCL_1045), LNCaP (RRID:CVCL_0395), VCaP (RRID:CVCL_2235), MyC-CaP (RRID:CVCL_J703), and TRAMP-C2 (RRID:CVCL_3615) cells were obtained from ATCC and tested negative for *Mycoplasma*. ARCaPM cells were obtained from Novicure. DU145, 22Rv1, and ARCaPM were grown in RPMI media with 10% FBS; LNCaP cells were grown in minimum essential media (IMEM) supplemented with 5% FBS and VCaP, MyC-CaP, and TRAMP-C2 cells were grown in Dulbecco's modified media supplemented with 10% FBS. Cells were grown at 37°C in a humidified atmosphere with 5% CO_2. The cells were screened for *Mycoplasma* every 1–2 months using a Myco-Sniff Mycoplasma PCR detection kit. Moreover, to avoid passage-dependent effects and ensure valid and reproducible experimental results, the cell passage number was kept under 30. To assess cell growth under steroid-depleted conditions, prostate cancer cells were cultured with phenol red-free media supplemented with 5% charcoal dextran-treated FBS. Syngenic mouse tumors generated from TRAMP-C2 and MyC-CaP cells were used to assess *in vivo* eIF3B effects on immune evasion and test the activity of combining 4EGI-1 (Selleckchem) with anti–PD-1 therapy (Bio X Cell; clone RMP1-14). Advanced prostate cancer xenograft models (PDX1, PDX2, and PDX3) generated from circulating tumor cells from prostate cancer patients previously characterized by our group (44, 52) were used in experiments to test the *in vivo* activity of 4EGI-1 alone or in combination with ADT. Organoid models were generated from two PDX models. Briefly, harvested PDX tumors were washed in PBS, minced in 10% RPMI media supplemented with antibiotics, and the cell suspension was filtered through a 70-μm cell strainer. The cells obtained by centrifuging at 1,300 rpm for 2 minutes were embedded into Matrigel (Corning) supplemented with growth medium to generate organoids. The cell viability of empty vector (EV; control) and eIF3B-overexpressing organoids cultured in regular FBS media and CS FBS media (phenol red–free) was determined by MTS Assay (Promega). For *in vivo* studies, about 500 organoids were subcutaneously injected into the

flanks of male NOD/SCID mice. Once the tumors reached a size of 200 mm^3, mice were surgically castrated to study the impact of eIF3B on castration resistance.

Bioinformatics Data Analysis

Transcriptomic profiles of prostate cancer tissues were obtained from the NCBI Gene Expression Omnibus database (GSE35988, GSE21032, GSE3933, and GSE84043; https://www.cancer.gov/tcga and https://github.com/cBioPortal/datahub/tree/master/public/prad_su2c_2019). Grasso and colleagues contain primary (n = 59) and warm autopsy (n = 35) samples (39). Taylor and colleague include primary (n = 131) and metastatic (n = 19) prostate cancer samples (40). Lapointe and colleagues include primary (n = 62) and metastatic (n = 9) prostate cancer samples (41). The Cancer Genome Atlas (TCGA) contains primary (n = 333) samples (50). Fraser and colleagues contain primary (n = 73) prostate cancer samples. SU2C contains metastatic (n = 444) samples (60). Differentially expressed genes between experimental conditions were determined by random permutation-based t test with a statistical significance cutoff of false discovery rate (FDR) <0.05. Modulation of molecular pathway gene sets and target gene signatures from the Molecular Signature Database (MSigDB; https://www.broadinstitute.org/msigdb) was determined by using a modified version of GSEA (84) and DAVID Bioinformatics Resources (https://david.ncifcrf.gov/) with a statistical significance cutoff of FDR <0.05. Pearson correlation analysis between *MITF* or *MITF A* and *eIF3B* mRNA expression was performed using R language with publicly available databases containing transcriptomic data from prostate cancer tissue samples. In addition, the association between *MITF* and *MITF* target gene signature with Gleason score was determined in patient datasets having Gleason annotation (Taylor and TCGA). The differential expression of *MITF* and its target gene signature in normal and tumor cells was assessed at single-cell level (45). As normalization was performed by original authors and the data were not integrated, no additional batch correction step was required for the datasets.

To define a gene signature that recapitulated the activation status of AR in prostate cancer, we used a previously identified gene set consisting of 31 genes (49). Briefly, we first selected 34 genes from a meta-analysis that described a set of genes that were consistently regulated by androgens in 6 different experimental studies (85). Based on the work by Massie and colleagues (86) and the Cancertool interface (87), we annotated these genes as induced or repressed by activated AR. The final signature comprised 23 genes consistently activated by androgens (upregulated: *ABCC4, ABHD2, ALDH1A3, APPBP2, DBI, DHCR24, DNAJB9, ELL2, FKBP5, HERC3, IQGAP2, KLK2, KLK3, KRT8, LIFR, MERTK, NDRG1, ODC1, PTPRM, SEC24D, SORD, TMPRSS2, TPD52*) and 8 that were repressed (downregulated: *BARD1, BCHE, CDK8, DDC, FN1, GATA2, MMP16, PIK3R3*), whereas 3 genes were excluded from the signature due to the inability to assign directionality. The AR signature was obtained by subtracting the average expression levels of the downregulated genes from the average expression levels of the upregulated genes per individual. Pearson correlation (r) was applied to analyze the relationship between *MITF* and *eIF3B* with the *AR* signature in patient samples from previously mentioned datasets using the cor.test function in R language.

To determine the correlation between eIF3B with T effector (*CD8a*, *GZMA*, and *GZMB*) and MHC-I (*TAP1*, *TAP2,* and *HLA-A*) signatures, we used genes reported previously (88, 89). The data used for the analysis were already quantified, and no raw data were processed. If in any case, the gene of interest is interrogated several times with several probes in case of the data retrieved by Microarray, the average expression was calculated of all available probes. The signatures were obtained by comparing the average expression levels of the genes per individual. Pearson correlation (r) was applied to analyze the relationship between *eIF3B* with the T effector or *MHC-I* signature in patient samples from datasets using the cor.test function in R language.

siRNA Knockdown

Predesigned Silencer Select (Ambion) siRNAs targeting control #1 (AM4636), *MITF* #1 (s8791) and #2 (s8792), *eIF3B* #1 (s16493) and #2 (s16494), *RRS1* #1 (s23296) and #2 (s23297), *TTL* #1 (s45441) and #2 (s45442), *SLC19A1* #1 (s13085) and #2 (s13086), *GPSM1* #1 (s25072) and #2 (s197865), *RANBP10* #1 (s33433) and #2 (s33434), *ATP6V0E1* #1 (s17155) and #2 (s225062), *TMEM243* #1 (s35655) and #2 (s35657), *FYCO1* #1 (s35795) and #2 (s35796), *GINM1* #1 (s41978) and #2 (s41979), and *ANXA4* #1 (s1389) and #2 (s1390) were transfected into cells seeded overnight at a density of 1×10^5 in 6-well plates. siRNAs and RNAiMAX lipofectamine (Invitrogen) were diluted in OptiMEM (Life Technologies), combined, and added dropwise to cells at a final concentration of 10 nmol/L. Knockdown efficiency was assayed 24 hours later by qPCR, and for each gene, the two most independently efficacious siRNAs were selected for further experiments.

Transcriptome Profiling of MITF-Knockdown Cells

To characterize the transcriptional program regulated by MITF, we performed RNA sequencing of prostate cancer models, DU145, 22Rv1, and ARCaPM, after 48 hours of being transfected with siRNA control or two siRNAs targeting MITF (biological replicates of n = 3 for each condition). High-quality total RNA samples (RNA Integrity score >8 by Agilent Bioanalyzer) were subjected to poly A–selected sequencing library preparation using TruSeq RNA Sample Prep Kit ver.2 (Illumina) following the manufacturer's protocol. The libraries were sequenced by HiSeq 2500 genome sequencer (Illumina) to generate 100 bp single-end reads. Data preprocessing and transcript abundance calculation (FPKM: fragments per kilo bases of exons for million mapped reads) were performed using TopHat and Cufflinks software using the human reference genome (hg19).

Focused Loss-of-Function Genetic Screen of Clinically Relevant MITF Target Genes

Custom siRNAs against 11 clinically upregulated genes were obtained from Ambion. For our screening system, we used the prostate cancer cell line models, DU145, 22Rv1, and ARCaPM. Efficacy of target gene depletion (mRNA decrease >80%) was tested by conventional qPCR using two independent siRNAs for each gene. Effects on colony formation was used to consider a target gene as a "hit." The following primers were used in the qPCR assay.

MITF: F-TGCCCAGGCATGAACACAC, R-TGGGAAAAATACACG CTGTGAG
eIF3B: F- CCGACCGACTTGAGAAACTC, R-TTCTTCACAGCATC CACAGC
RRS1: F-ACACGCAACTGCTCATCAAC, R-TCTTCTTCTTGGGA CGGATG
TTL: F-CATAGACAACCAGGGCCAAG, R-GGTTCTGAAGCAGT CCGAAG
SLC19A1: F-ACCTCGTGTGCTACCTTTGC, R-GGTAGTCGGTG AGCAGGAAC
GPSM1: F-CCTCAGAGAAGCCTGACCTG, R-GGTACTTCCTGCT CCTCACG
RANBP10: F-CCCTATGGTCCCACATTCAC, R-ACAATCTCCCCA GGTGTCTG
ATP6V0E1: F-CCTCACTGTGCCTCTCATTG, R-GTTGAGTTGG GCCAGAATTG
TMEM243: F-TTTGCTACCAGGACCTACGG, R-CAACGGTTTTG GAGGTAGTTG
FYCO1: F-GTGACCTGGAGGAGCAGAAG, R-TGCAGACTGGAG TTCACAGG

GINM1: F-ACCCTCCCTTTGGAAGAAAG, R-ATATGAAGATGGC GGCTCTG
ANXA4: F-GACGGAGCCTTGAAGATGAC, R-GTCCCCCATTTC TTCTCTCC

Identification of Predicted MBEs

Evolutionarily conserved MBEs in the human *eIF3B* promoter were identified computationally using multiple sequence alignment software (90) and the EPD database (91). Multiple gene sequences containing the *eIF3B* promoter regions were analyzed using the Jaspar database with cutoff *P* value of 0.001. The following oligonucleotides were used in cloning and qPCR to further study the identified MBEs in the transcriptional regulation of eIF3B by MITF.

MITF MBE1 ChIP qPCR:
F-ACAGGGTCTCGCTATGTTGC
R-TGTACTTGATGCCACTGAACTG

MITF MBE23 ChIP qPCR:
F-TTAAGACATCCCCCAACCAG,
R-GGGCTTTCACAGTGGTTCAG

MITF MBE4 ChIP qPCR:
F-GAAAGGAAAGGGGGAGGAC
R-GCCCGAAAATCATCAAACTG

MITF MBE5 ChIP qPCR:
F-GAGTCCTCTCAGGGTCGTTC
R-CTACAGCCCAGCCATGTG

Negative control ChIP qPCR:
F-AAACCACTGCTCAATGAAATAAAAG
R-TTTTTCCAATTCTGTGAAGAAAGTC

MITF MBE2-mutant cloning:
F-AGATAGAAGCaaaataCACCCAATGCC
R-GGCATTGGGTGtattttGCTTCTATCT

MITF MBE3-mutant cloning:
F-CCCCCGCCCCaaaataACCCGCGCTGTCCCG
R-CGGGACAGCGCGGGTtattttGGGGCGGGGG

Molecular Cloning

The *eIF3B* promoter sequence (−1,400 to +200 nucleotides) was purchased at GenScript and cloned into the pGL4.10 reporter vector using NheI and BglII sites (Promega). The resulting vector was used as a template to mutate MITF-binding sequences by site-directed mutagenesis. After synthesizing the mutant strand by PCR, the template sequence was digested with *Dpn*I restriction enzyme for 2 hours at 37°C. The mutant vector was transformed into competent cells for nick repair, plasmid DNA was recovered, and mutation of the binding site was confirmed by Sanger sequencing.

ChIP

ChIP-seq was carried out as previously described (92) on MITF immunoprecipitated (Active Motif antibody; RRID:AB_2614955) 22Rv1 DNA samples at the Genome Analysis Core, Mayo Clinic, Rochester, MN. Briefly, paired-end libraries were prepared using Chip-derived DNA according to the manufacturer's instructions for the NEBNext Ultra II library prep kit (New England BioLabs). The concentration and size distribution of the completed libraries were determined using an Advanced Analytical Fragment Analyzer (Agilent Technologies Inc.) and Qubit fluorometry (Thermo Fisher Scientific Inc). Libraries were sequenced (6 samples/P2 Flow cell) following Illumina's standard protocol using the Illumina NextSeq 2000 and P2 flow cell. The flow cells were sequenced as 50 × 2 paired-end reads using NextSeq 1000/2000 Control Software Suite v1.4.1 and RTA3.

MITF ChIP followed by qRT-PCR was performed as previously described (93). Briefly, chromatin from cross-linked DU145, 22Rv1, and ARCaPM cells was sonicated, precleared, and incubated overnight with 5 μg of the corresponding antibody in RIPA buffer and precipitated with protein G/A-Sepharose. The DNA–protein–antibody complexes were then washed three times with RIPA, three times with RIPA- NaCl, twice with Lithium Buffer, and twice with 1× TE. Cross-linkage of the coprecipitated DNA–protein complexes was reversed and the immunoprecipitated DNA was analyzed by qPCR.

eIF3B Promoter Luciferase Reporter Assay

DU145, 22Rv1, and ARCaPM cells were seeded into 12-well plates at a density of 1.25×10^5 and allowed to attach overnight. A transfection mix was prepared by combining 198 ng of pGL4.10 or pGL4.10-eIF3B promoter, MBE2 or MBE4, 19.8 ng of pRL-Renilla, and 882 ng of an MITFA expression vector or GFP control, or siRNA control or two siRNAs against MITF. Luciferase activity was measured with a Dual-Luciferase-Assay kit (Promega) 48 hours after transfection, mixing 50 μL of lysate with 50 μL of Luciferase Buffer Assay and analyzed in an automatic luminometer. 50 μL of Stop & Glo reagent was then added and Renilla luminescence was measured after 10 minutes of incubation. Ratios of Firefly versus Renilla luciferase were calculated to determine promoter activity.

eIF3B eCLIP

eCLIP studies were performed by Eclipse Bioinnovations Inc https://eclipsebio.com/ according to the published single-end eCLIP protocol (94) with the following modifications. Approximately 5×10^7 22Rv1 cells per sample were grown and UV cross-linked at 400 mJoules/cm^2 with 254 nm radiation, flash frozen, and stored until use at −80°C. Cells were lysed using 1 mL of eCLIP lysis mix and subjected to one round of sonication for 5 minutes with 30 seconds ON/OFF (total 10 minutes) at 75% amplitude. Rabbit Anti-eIF3B/EF3S9 antibody was then precoupled to Anti-Rabbit IgG Dynabeads, added to lysate, and incubated overnight at 4°C. Prior to immunoprecipitation, 2% of the sample was taken as the paired input sample, with the remainder magnetically separated and washed with eCLIP high stringency wash buffers. IP and input samples were cut from the membrane at the relative band size to 75 kDa above. RNA adapter ligation, IP-Western, reverse transcription, DNA adapter ligation, and PCR amplification were performed as previously described. The eCLIP cDNA adapter contains a sequence of 10 random nucleotides at the 5′ end. This random sequence serves as a unique molecular identifier (UMI; ref. 95) after sequencing primers are ligated to the 3′ end of cDNA molecules. Therefore, eCLIP reads begin with the UMI and, in the first step of analysis, UMIs were pruned from read sequences using umi_tools (v0.5.1; ref. 96). UMI sequences were saved by incorporating them into the read names in the FASTQ files to be utilized in subsequent analysis steps. Next, 3′ adapters were trimmed from reads using cutadapt (v2.7; http://journal.embnet.org/index.php/embnetjournal/article/view/200), and reads shorter than 18 bp in length were removed. Reads were then mapped to a database of human repetitive elements and rRNA sequences compiled from Dfam (97) and Genbank (98). All nonrepeat mapped reads were mapped to the human genome (hg38) using STAR (v2.6.0c; ref. 99). PCR duplicates were removed using umi_tools (v0.5.1) by utilizing UMI sequences from the read names and mapping positions. Peaks were identified within eCLIP samples using the peak caller CLIPper (https://github.com/YeoLab/clipper; ref. 100). For each peak, IP versus input fold enrichment values were calculated as a ratio of counts of reads overlapping the peak region in the IP and the input samples (read counts in each sample were normalized against the total number of reads in the sample after PCR duplicate removal).

A *P* value was calculated for each peak by the Yates' Chi-square test, or Fisher exact test if the observed or expected read number was below 5. Comparison of different sample conditions was evaluated in the same manner as IP versus input enrichment; for each peak called in IP libraries of one sample type, we calculated enrichment and *P* values relative to normalized counts of reads overlapping these peaks in another sample type. Peaks were annotated using transcript information from GENCODE (101) with the following priority hierarchy to define the final annotation of overlapping features: protein-coding transcript (CDS, UTRs, and intron), followed by noncoding transcripts (exon and intron). Enrichment of motifs in the eCLIP peaks was determined with the HOMER suite.

Cloning of U/C-Rich Motif Containing 5′UTRs in the Luciferase Reporter Vector

The *AR* and *HLA-A* 5′UTR regions identified to bind eIF3B via eCLIP-seq were cloned into luciferase reporter plasmid pGL3. The pGL3 vector was digested with *Nco*I, which cuts immediately upstream of the luciferase translation start site. The AR and HLA-A 5′ UTRs were synthesized (GenScript) and subcloned into the linearized pGL3 vector. The WT and deleted (MUT) U/C-rich motif in the AR and HLA-A 5′ UTRs were sequence validated (GenScript).

U/C-Rich Luciferase Reporter Assay

22Rv1 cells seeded in 6-well plates (2×10^5 cells/well) in RPMI media. After 24 hours, cells were transfected with either empty pGL3 vector, WT U/C-rich 5′UTR (WT), or deleted U/C-rich (MUT) 5′UTR pGL3 vectors and Renilla vector. Cells were collected 24 hours after transfection and split in two for either RNA extraction (Qiagen RNeasy kit) and normalization by qPCR, or for protein extraction for luciferase activity assay measure following the manufacturer's instructions (Dual-Luciferase-Assay kit, Promega). Luminescence was detected and analyzed in an automatic luminometer (Promega GloMax Luminometer). Firefly luciferase activity was normalized to Renilla luciferase activity comparing WT and mutant 5′UTRs vectors. The translation efficiency of the Firefly reporter construct was calculated by normalizing Firefly luciferase RNA to Renilla luciferase and relative to WT plasmid.

Polysome Profiling

Polysome profiling was also carried out following a previously described protocol with minor modifications (102). Briefly, indicated cells were collected after treating with cycloheximide (100 μg/mL) and lysed by resuspending in lysis buffer (10 nmol/L Tris, pH 7.4, 100 mmol/L NaCl, 1 mmol/L DTT, 20 mmol/L $MgCl_2$, 500 μg/mL heparin, and 100 μg/mL cycloheximide). A 5%–50% sucrose gradient (w/v) was made with a buffer (50 nmol/L Tris Acetate pH 7.0, 50 mmol/L NH_4Cl, 10 mmol/L $MgCl_2$, 1 mmol/L DTT), and a clarified cell lysate was carefully loaded on top. The gradients were then centrifuged at 23,460 × *g* for 3 hours at 4°C in a Beckman SW-41ti rotor. The fractions were obtained and the OD255 of each fraction was noted. The same volume of RNA extracted from the fractions was used in cDNA synthesis. The target mRNAs in the fractions were quantified by qPCR. The qPCR data were analyzed by the threshold cycle (Ct) comparative method and quantified as a percentage of the total RNA considering the whole fractions stand for 100% (103).

eIF3B UV-RIP

eIF3B RIP assay was performed as previously reported by Lee and colleagues (34). Briefly, 10^7 cells from DU145, 22Rv1, and ARCaPM shRNA control or shRNA MITF #1 and #2 UV (400 mJ/cm^2) cross-linked using a Stratalinker UV-light box were harvested by scrapping and resuspended in two volumes of NP40 lysis buffer. The lysates were incubated with either rabbit IgG or rabbit anti-eIF3b antibody and protein G Dynabeads (Invitrogen) for 2 hours at 4°C. The beads were washed five times with NP40 buffer (50 mmol/L HEPES-KOH pH 7.5, 500 mmol/L KCl, 2 mmol/L EDTA, 1% Nonidet P-40 alternative, 0.5 mmol/L DTT), and bound RNAs were isolated by phenol-chloroform extraction and ethanol precipitation. cDNA was reverse transcribed using the Superscript III kit, and qPCR was performed using SYBR Green.

Puromycin Assay

Quantification of the global protein synthesis rate of prostate cancer cells was evaluated using the surface sensing of translation (SunSEt) method as previously described (104). Puromycin is a structural analogue of aminoacyl-transfer RNA (aminoacyl-tRNA) and, as such, can be incorporated into elongating peptide chains via the formation of a peptide bond (105). Cells were incubated with puromycin (Gibco) 1 μmol/L for 6 hours at 37°C in a humidified atmosphere with 5% CO_2. Immunologic detection of puromycin-labeled peptides using an antibody against puromycin was then assessed following the standard immunoblot procedure. For *in vivo* experiments, mice were sacrificed, and tumors were harvested after 60 minutes of an intraperitoneal injection of 200 μL of 2.5 mmol/L puromycin and levels of puromycin-labeled peptides in tumors measured by IHC using the antibody against puromycin (Millipore; RRID:AB_2566826).

shRNAs, CRISPR/Cas9 Knockout, and Gene Overexpression

For inducible shRNA-mediated inhibition of MITF, two clones (MITF.763 and MITF.2397) were selected following the screen of a custom library. A control shRNA targeting Renilla luciferase was also used. Predictions of shRNA were obtained using "sensor rules" to enrich for predictions harboring sequence features associated with effective shRNAmir processing and potent knockdown (106). DU145, 22Rv1, ARCaPM, LNCaP, VCaP, MyC-Cap, and TRAMP-C2 cells were infected with a lentivirus containing a TRIN-E vector with the control or MITF-targeting shRNAs and selected with neomycin (0.4 mg/mL). MITF depletion efficiency was evaluated by immunoblotting. Vectors were designed by Dr. Amaia Lujambio (Mount Sinai School of Medicine, NY, USA). Studies with stably expressing shRNA sublines were performed with pools passaged no more than five times.

Genome editing of *MITFA, H2-K1*, and *H2-D1* were performed with the CRISPR/Cas9 system. Briefly, sgRNA targeting *MITFA* were purchased from GenScript and subcloned into lentiCRISPRv2 vector (Addgene 52961) following a rigorous method to exclude potential off-target effects of sgRNA. Prostate cancer cells were transduced with viral particles of EV or sgRNA *MITFA*#1 (ATCGTGCCGGATTTCGAAGT), *H2-K1* (CCTCGGGGAGCCCCGGTACA), and *H2-D1* (GGTGACTTCACCTTTAGATC). Cells were then processed for subsequent analyses by qPCR and immunoblotting.

Overexpression of MITFA, eIF3B, and 4E-BP1 (Addgene) was conducted by transducing indicated vectors in prostate cancer cells.

Cell Population Doubling Assays

Proliferation capacity of prostate cancer cells was performed by plating 10^4 cells in 60-mm culture dishes and counting the number of cells at indicated time points using an automated cell counter (Countess II Life Technologies).

Mouse Intracardiac Injections

Intracardiac injections were performed as previously described (44). Briefly, the ventral thorax of 3- to 4-week-old mice was shaved prior to anesthesia with an isoflurane vaporizer and nose cone. The thorax was sterilized with iodine and alcohol and a sterile marker

was used to mark a location halfway between the sternal notch and the xyphoid process. 100 μL from a 1 × 10^6 cells/mL suspension of tumor cells in sterile 1× PBS was drawn into a 30.5-gauge needle. The upright syringe was gently inserted through the mark and for each injection successful penetration into the left ventricle was confirmed visually by a pulse of bright red blood into the syringe. Following each experiment, a detailed necropsy was performed to confirm the disseminated tumor burden grossly and histologically.

In Vivo *Mouse Model Therapy*

For *in vivo* studies involving testing the efficacy of combining a translation inhibitor (4EGI-1) with ADT or an ICI anti–PD-1, two *in vivo* experimental models, including subcutaneous and intracardiac injections of prostate cancer cells, were performed. Subcutaneous xenografts were generated by implantation of 10^6 indicated prostate cancer cells or 500 organoids generated from PDX in a 1:1 mixture of growth medium and Matrigel (Corning) into the flanks of NOD/SCID mice. When subcutaneous tumors became palpable, mice were randomly assigned to treatment groups containing five animals. Intracardiac injection of prostate cancer cells was performed as described above.

To study the contribution of MITF depletion and eIF3B overexpression on castration resistance, intact and castrated mice were used. For assessing combined therapy efficacy castrated mice were treated with vehicle (DMSO) or 4EGI-1 (75 mg/kg/i.p. 5 days a week). The vehicle was 10% DMSO in sterile 1× PBS.

To study the extent of eIF3B contribution to immune evasion, mice bearing tumors from vector control or eIF3B-overexpressing cells were either treated with Poly(I:C) (2.5 mg/kg, intratumoral, Tocris) or anti–PD-1 antibody (250 μg/mouse, i.p.). Drugs were administered on alternate days for 2 weeks and tumors were harvested 2 days after the final treatment. For combined therapeutic efficacy studies, indicated tumor-bearing mice were divided into four equal groups and intraperitoneally administered with control (DMSO and IgG), 4EGI-1 (75 mg/kg/i.p. 5 days a week), anti–PD-1 (250 μg/mouse/i.p., once every 2 days) or 4EGI-1 + anti–PD-1. CD8 T lymphocytes were depleted by administering 400 μg of anti-CD8α (clone 2.43, Bio X Cell) i.p. twice weekly beginning 1 day prior to therapy. Tumor size was measured at regular intervals. At the end of the study, tumors were harvested, weighed, and subjected to IHC analysis.

Monitoring Subcutaneous Tumor Growth

Subcutaneous tumors were generated by implantation of indicated prostate cancer cells or organoids generated from PDX in a 1:1 mixture of culture medium and Matrigel (Corning) into the flanks of mice. Tumor dimensions were monitored weekly using Vernier calipers. Tumor volume was calculated according to the formula $V = (a^2 \times b)/2$, where a and b are the minimal and maximal diameters in millimeters, respectively. In accordance with institutional guidelines, mice bearing subcutaneous tumors greater than 500 mm^3 were sacrificed. Explanted tumors were weighed, formalin-fixed, and embedded in paraffin for IHC analysis.

In Vivo *Bioluminescence Imaging*

Imaging was performed using an IVIS Spectrum (Xenogen) imager. Animals received luciferin (PerkinElmer) at 200 μg/kg by i.p. injection 2 minutes prior to imaging. Animals were then anesthetized using an isoflurane vaporizer and placed onto the warmed stage inside the camera box. At this stage, animals received continuous exposure to 2% isoflurane (Piramal). For quantification, rectangular regions of interest incorporating the entire animal were measured. The signal was measured in photons per second using Living Image software v.4.2.

General Toxicity Monitoring

Body weights for every mouse were recorded every 3 days, and fluctuations were computed by the percentage of current body weight relative to baseline. When animals showed signs of weight loss therapy was discontinued. In accordance with institutional guidelines, all animals experiencing greater than 20% weight loss were sacrificed.

RNA Extraction and qPCR

RNA was isolated using the RNeasy Mini kit (Qiagen) in accordance with the manufacturer's instructions. Complementary DNA was synthesized from equivalent concentrations of total RNA using the SuperScript III First-Strand Synthesis SuperMix Kit (Invitrogen) as per the manufacturer's instructions. Amplification was carried out using a Proflex PCR System (Applied Biosystems). Cycle threshold values were determined and normalized to the loading control for each experiment. Fold changes for experimental groups relative to respective controls were calculated using Proflex software (Applied Biosystems). Primers used in the qPCR assay are:

AR: F-CTTCGAATGAACTACATCAAGGAAC, R-CTTGATTAGCAGGTCAAAAGTGAAC
KLK3: F-CACAGGCCAGGTATTTCAGGT, R-GAGGCTCATATCGTAGAGCGG
TMPRSS2: F-GTCCCCACTGTCTACGAGGT, R-CAGACGACGGGGTTGGAAG
Luciferase: F-ATCCGGAAGCGACCAACGCC, R-GTCGGGAAGACCTGCCACGC
HLA-A: F-TGTCTTCCCAGCCCACCATCC, R-CATCACGGCAGCGACCACAG
HLA-B: F-CCCAGTCCACCGTCCCCATC, R-CACATCACAGCAGCGACCACAG
HLA-C: F-TCTACCCTGCGGAGATCACACTG, R-GCTCTTGTCCAGAAGGCACCAC
H2-K: F-GCCTCCTCCATCCACTGTCTCC, R-CCCCTCCTTTTCCACCTGTGTTTC
H2-D: F-GAGTATTGGGAGCGGGAAACACAG, R-AGTAGCCGAGCAGGTTCCTCAG
H2-L: F-CACCCTGACCTGGCAGTTGAATG, R-TCCCAAGAGGCACCACCACAG
Mouse *GAPDH*: F-ACTCCACTCACGGCAAATTC, R-TCTCCATGGTGGTGAAGACA
β-actin: F-AAACTGGAACGGTGAAGGTG, R-GTGGCTTTTAGGATGGCAAG
MITF M spliced: F-CATTGTTATGCTGGAAATGCTAGAA, R-GGCTTGCTGTATGTGGTACTTGG

MITF A, *-C*, *-H,* and *-J* primers were from Hershey and Fisher (107).

Immunoblot and Immunoprecipitation

Whole-cell extracts were prepared in RIPA buffer (Invitrogen) and analyzed by immunoblot using standard procedures. Extracts from PDX tumors were obtained using a tissue homogenizer (Fisher Scientific). For immunoprecipitation, extracts were incubated with the indicated antibodies overnight at 4°C. Following 2 hours of incubation with protein A/G Dynabeads (Invitrogen), beads were washed four times, resuspended in 1 × Laemmli sample buffer and boiled for 5 minutes. After protein quantification using the BCA method, 5× Laemmli buffer was added, and the mix was boiled for 5 minutes. SDS-PAGE resolved proteins were transferred to PVDF membranes and incubated with primary antibodies. The various other primary antibodies used in the study were MITF (Sigma; RRID:AB_1079381 and Abcam; RRID:AB_470315), AR (Abcam; RRID:AB_2861275), eIF3B (Abcam; RRID:AB_941410 and Bethyl; RRID:AB_1210997), eIF3D (Bethyl; RRID:AB_1210973), eIF3C (Novus; RRID:AB_2096744), eIF3E (Bethyl; RRID:AB_10749034), eIF3K (Abcam; RRID:AB_1924951), eIF3G (Bethyl), eIF3F (Bethyl;

RRID:AB_10748371), eIF3h (Bethyl; RRID:AB_1210983), RPL23A/uL23 (Bethyl; RRID:AB_2615652), RPS24/eS24 (Bethyl; RRID:AB_2620193), RPS19/eS19 (Bethyl; RRID:AB_2620351), eIF4E (BD; AB_397664), eIF4G (Bethyl), cleaved-PARP (Cell Signaling Technology), p70S6K (Cell Signaling Technology; RRID:AB_2800283), p4E-BP1 (Cell Signaling Technology; RRID:AB_823413), 4E-BP1 (Cell Signaling Technology; RRID:AB_659944), cleaved-caspase 3 (Cell Signaling Technology; RRID:AB_2341188), and GAPDH (Abcam; RRID:AB_1267174). Secondary antibodies were used at 1:2,000.

AR Protein Half-life

To evaluate whether eIF3B overexpression affects AR half-life, we carried out an AR protein stability experiment. To this end, EV (control) and eIF3B-overexpressing 22Rv1 cells were treated with cycloheximide (100 μg/mL) and samples were collected at 0, 2, 4, 8, and 12 hours after cycloheximide treatment. The AR protein expression in Western blots was quantified by using ImageJ software.

PROTAC Degrader

The extent of the contribution of AR to eIF3B-mediated oncogenic phenotype was further verified using ARV-110 (Selleckchem), an AR PROTAC degrader in LNCaP and VCaP hormone-sensitive cells. The cells were treated with ARV-110 (20 ng/mL), and cell population doubling was measured at indicated time points as described above.

Single-Cell Mass Cytometry (Cytometry by Time of Flight)

Cytometry by time of flight (CyTOF) was used to quantify the tumor immune cell infiltration by labeling selected surface and intracellular targets (108). Briefly, single-cell suspensions were prepared from the tumor samples, and the red blood cells (RBC) were removed by using RBC lysis buffer. Anti-mouse CD45 (89Y tag), anti-mouse CD3e (152Sm tag), anti-mouse CD8a (153-Eu tag), anti-mouse CD4 (145-Nd tag), anti-mouse CD11by (172-Yb tag), anti-mouse NK1.1 (170Er tag), anti-mouse Ly-6G (141Pr tag), anti-mouse Ly-6C (162Dy tag), and anti-mouse granzyme B (173Yb tag) antibodies from Fluidigm were used. Cells were first stained for surface markers by incubating with the fluorophore-conjugated antibodies for 45 minutes at room temperature. Following fixation and permeabilization, cells were stained for intracellular marker(s). The data were acquired on a CyTOF instrument (Fluidigm) in the Flow Cytometry and Cellular Imaging Core Facility at Mayo Clinic, Rochester. The data were analyzed with cytofkit package and PhenoGraph in R studio as described elsewhere (108).

Flow Cytometry

Single-cell suspension of the tumor samples was prepared by mechanical dissociation. Cells were stained first with Alexa Fluor 647 anti-CD8α (BioLegend; RRID:AB_2563452). Following fixation and permeabilization, the cells were stained with Alexa Fluor 594 anti–granzyme B (Antibodies-online). Each antibody was incubated for 30 minutes on ice avoiding exposure to light. MHC-I expression was analyzed in mouse cell lines stained with PE MHC class I (Invitrogen; RRID:AB_466122). The data were acquired on BD Fortessa X20 flow cytometer and analyzed using FlowJo v10.8.1.

IHC

IHC analyses were conducted on prostate cancer FFPE tissue sections from human samples, PDXs, and syngenic mouse tumors. Tissue sections (5 μm) were deparaffinized and submitted to standard peroxidase-based IHC procedures. MITF (Abcam), AR (Abcam), Caspase-3 (Abcam; RRID:AB_2069705), CD3 (Abcam; RRID:AB_443425), CD8 (Cell Signaling Technology; RRID:AB_2756376), and granzyme B (Abcam; RRID:AB_2114427) quantification of positive cells was determined by counting the number of tumor cells in 10 contiguous high-power fields in three different areas of each section and referred to the total number of counted cells. eIF3B (Bethyl), MHC-I (Invitrogen; RRID:AB_2899999), and puromycin (Millipore) staining intensity was scored as low (– or +) and high (++) in three different areas of each tumor section.

Proximity Ligation Assay

The *in situ* Duolink Proximity Ligation Assay (PLA; Sigma) was used to detect eIF4E–eIF4G or eIF4E–eIF3B interactions in FFPE prostate cancer tissue sections and cultured prostate cancer cells. Dissociating effects of 4EGI-1 on eIF4E and eIF4G or eIF4E and eIF3B translation initiation subunits binding were tested on prostate cancer cells and tumors generated in mice. Prostate cancer cells were treated with 4EGI-1 5 μmol/L for 24 hours and mice were treated with 4EGI-1 75 mg/kg/i.p. for 5 days.

FFPE sections were deparaffinized, rehydrated, and subjected to antigen retrieval following standard methods. Tissue samples were blocked for 30 minutes and incubated overnight at 4°C with eIF4E, eIF4G, and eIF3B primary antibodies. Prostate cancer cells were grown on coverslips and after 24-hour exposure to vehicle or 4EGI-1 washed and fixed with 10% formalin for 30 minutes at room temperature. Next, cells were permeabilized with 0.25% Triton-X100 for 10 minutes at room temperature and blocked for 1 hour at 37°C before incubation with eIF4E, eIF4G, and eIF3B primary antibodies for 2 hours at room temperature. Following primary antibody incubation, PLA signal was assessed following the manufacturer's protocol. Briefly, both tissue sections and prostate cancer cells were incubated with secondary antibodies conjugated to oligonucleotides (PLA plus/minus probes) for 1 hour at 37°C. The two hybridized oligonucleotides were joined in a closed circle using a ligase at 37°C for 30 minutes. The DNA was then amplified with rolling circle amplification, and detection of the amplicons was carried out using the Brightfield detection kit. The number of PLA signals per cell was counted using ImageJ.

Quantification and Statistical Analysis

Statistical analysis was carried out with SPSS version 19.0 (SPSS, Inc.). To analyze correlations, we used Pearson correlation tests when the two variables were assessed as continuous, *t* test when one variable was assessed as continuous and the other as qualitative and χ^2 test (Fisher exact test) when the two variables were qualitative. Survival analyses were performed using the Kaplan–Meier method and curves were compared by the log-rank test. All the statistical tests were conducted at the two-sided 0.05 level of significance.

Data and Software Availability

The accession numbers for the datasets generated in this study include RNA sequencing MITF knockdown in prostate cancer cells (GEO: GSE133977), MITF ChIP-seq in prostate cancer cells (GEO: GSE237870), and eIF3B eCLIP-seq in prostate cancer cells (GEO: GSE240338).

Transcriptomic profiles of prostate cancer tissues were obtained from the NCBI Gene Expression Omnibus database (GSE35988, GSE21032, GSE3933, and GSE84043; https://www.cancer.gov/tcga, https://github.com/cBioPortal/datahub/tree/master/public/prad_su2c_2019, and https://ega-archive.org/datasets/EGAD00001008340).

Authors' Disclosures

D.P. Petrylak reports personal fees from Ada Cap (Advanced Accelerator Applications), Amgen, Astellas, AstraZeneca, Bayer, Bicycle Therapeutics, Boehringer Ingelheim, Bristol Myers Squibb, Clovis Oncology, Eli Lilly, Exelixis, Gilead Sciences, Incyte, Infinity Pharmaceuticals, Ipsen, Janssen, Merck & Company Inc., Mirati,

Monopteros, Pfizer, Pharmacyclics, Regeneron, Roche, Sanofi-Aventis, Seattle Genetics, and Urogen, and grants from Ada Cap (Advanced Accelerator Applications), Agensys Inc., Arvinas, Astellas, AstraZeneca, Bayer, BioXcel Therapeutics, Bristol Myers Squibb, Clovis Oncology, Daiichi Sankyo Company Limited, Eisai, Eli Lilly, Endocyte, Ferring, Genentech, Gilead Sciences, Innocrin, MedImmune, Medivation, Merck, Mirati, Novartis, Pfizer, Progenics, Replimune, Roche, Sanofi-Aventis, and Seattle Genetics during the conduct of the study. A. Lujambio reports grants from Pfizer and Genentech outside the submitted work. Y. Hoshida reports personal fees from Helio Genomics and Roche Diagnostics, personal fees and other support from Espervita Therapeutics, and other support from Alentis Therapeutics outside the submitted work. No disclosures were reported by the other authors.

Authors' Contributions

Y. Hoshida: Resources, data curation, software, supervision, methodology, writing–original draft, writing–review and editing. **S. Zhu:** Data curation, software, formal analysis, validation, investigation, visualization, methodology, writing–original draft, writing–review and editing. **V. Jawalagatti:** Data curation, formal analysis, validation, investigation, visualization, methodology, writing–original draft, writing–review and editing. **M. Carceles-Cordon:** Resources, data curation, formal analysis, validation, investigation. **A. Ertel:** Resources, data curation, software, formal analysis, validation, investigation, visualization, methodology, writing–original draft, writing–review and editing. **S. Garcia-Longarte:** Resources, data curation, software, formal analysis, validation, investigation. **W.-M. Song:** Formal analysis, visualization, methodology. **N. Fujiwara:** Software, formal analysis, methodology. **P. Li:** Supervision, validation, investigation, methodology. **I. Mendizabal:** Data curation, software. **D.P. Petrylak:** Visualization, methodology. **W.K. Kelly:** Visualization, methodology. **E.P. Reddy:** Visualization, methodology. **L. Wang:** Software, formal analysis. **M.J. Schiewer:** Visualization, methodology. **A. Lujambio:** Visualization, methodology. **J. Karnes:** Visualization, methodology. **K.E. Knudsen:** Visualization, methodology. **C. Cordon-Cardo:** Resources, visualization, methodology. **H. Dong:** Resources, supervision, visualization, methodology. **H. Huang:** Resources, supervision, visualization, methodology. **A. Carracedo:** Software, formal analysis, visualization, methodology. **S. Santasusagna:** Conceptualization, resources, data curation, formal analysis, supervision, funding acquisition, validation, investigation, visualization, methodology, writing–original draft, project administration, writing–review and editing. **V. Rodriguez-Bravo:** Conceptualization, resources, data curation, formal analysis, supervision, funding acquisition, validation, investigation, visualization, methodology, writing–original draft, project administration, writing–review and editing. **J. Domingo-Domenech:** Conceptualization, resources, data curation, formal analysis, supervision, funding acquisition, validation, investigation, visualization, methodology, writing–original draft, project administration, writing–review and editing.

Acknowledgments

J. Domingo-Domenech is funded by NIH/NCI R01 CA261925. V. Rodriguez-Bravo is funded by NIH/NCI R01 CA237398. We thank Dr. Andrew E. Aplin, Dr. Christine Eischen, Dr. Elda Grabocka, and Dr. Ya-Ming Hou for sharing reagents and fruitful discussion on this project. Finally, we thank the Philadelphia Prostate Cancer Biome Project for its support of this project and Dr. Edward Gerner for philanthropic support of this study.

The publication costs of this article were defrayed in part by the payment of publication fees. Therefore, and solely to indicate this fact, this article is hereby marked "advertisement" in accordance with 18 USC section 1734.

Note

Supplementary data for this article are available at Cancer Discovery Online (http://cancerdiscovery.aacrjournals.org/).

Received March 15, 2023; revised July 28, 2023; accepted September 5, 2023; published first September 7, 2023.

REFERENCES

1. Labrie M, Brugge JS, Mills GB, Zervantonakis IK. Therapy resistance: opportunities created by adaptive responses to targeted therapies in cancer. Nat Rev Cancer 2022;22:323–39.
2. Konieczkowski DJ, Johannessen CM, Garraway LA. A convergence-based framework for cancer drug resistance. Cancer Cell 2018;33:801–15.
3. Sung H, Ferlay J, Siegel RL, Laversanne M, Soerjomataram I, Jemal A, et al. Global cancer statistics 2020: GLOBOCAN estimates of incidence and mortality worldwide for 36 cancers in 185 countries. CA Cancer J Clin 2021;71:209–49.
4. Carceles-Cordon M, Kelly WK, Gomella L, Knudsen KE, Rodriguez-Bravo V, Domingo-Domenech J. Cellular rewiring in lethal prostate cancer: the architect of drug resistance. Nat Rev Urol 2020;17:292–307.
5. Davies AH, Beltran H, Zoubeidi A. Cellular plasticity and the neuroendocrine phenotype in prostate cancer. Nat Rev Urol 2018;15:271–86.
6. Shen MM, Abate-Shen C. Molecular genetics of prostate cancer: new prospects for old challenges. Genes Dev 2010;24:1967–2000.
7. Hemesath TJ, Steingrimsson E, McGill G, Hansen MJ, Vaught J, Hodgkinson CA, et al. Microphthalmia, a critical factor in melanocyte development, defines a discrete transcription factor family. Genes Dev 1994;8:2770–80.
8. Bambury RM, Battley JE, McCarthy A, Brady C, O'Reilly S, Kelly PJ, et al. Translocation renal cell carcinomas: an evolving entity and a member of the microphthalmia transcription factor-associated family of tumors. Clin Genitourin Cancer 2013;11:357–61.
9. Skala SL, Xiao H, Udager AM, Dhanasekaran SM, Shukla S, Zhang Y, et al. Detection of 6 TFEB-amplified renal cell carcinomas and 25 renal cell carcinomas with MITF translocations: systematic morphologic analysis of 85 cases evaluated by clinical TFE3 and TFEB FISH assays. Mod Pathol 2018;31:179–97.
10. Steingrimsson E, Copeland NG, Jenkins NA. Melanocytes and the microphthalmia transcription factor network. Annu Rev Genet 2004;38:365–411.
11. Steingrimsson E, Moore KJ, Lamoreux ML, Ferre-D'Amare AR, Burley SK, Zimring DC, et al. Molecular basis of mouse microphthalmia (mi) mutations helps explain their developmental and phenotypic consequences. Nat Genet 1994;8:256–63.
12. Garraway LA, Widlund HR, Rubin MA, Getz G, Berger AJ, Ramaswamy S, et al. Integrative genomic analyses identify MITF as a lineage survival oncogene amplified in malignant melanoma. Nature 2005;436:117–22.
13. Hoek KS, Schlegel NC, Brafford P, Sucker A, Ugurel S, Kumar R, et al. Metastatic potential of melanomas defined by specific gene expression profiles with no BRAF signature. Pigment Cell Res 2006;19:290–302.
14. Hoek KS, Eichhoff OM, Schlegel NC, Dobbeling U, Kobert N, Schaerer L, et al. In vivo switching of human melanoma cells between proliferative and invasive states. Cancer Res 2008;68:650–6.
15. Konieczkowski DJ, Johannessen CM, Abudayyeh O, Kim JW, Cooper ZA, Piris A, et al. A melanoma cell state distinction influences sensitivity to MAPK pathway inhibitors. Cancer Discov 2014;4:816–27.
16. Muller J, Krijgsman O, Tsoi J, Robert L, Hugo W, Song C, et al. Low MITF/AXL ratio predicts early resistance to multiple targeted drugs in melanoma. Nat Commun 2014;5:5712.
17. Davis IJ, Kim JJ, Ozsolak F, Widlund HR, Rozenblatt-Rosen O, Granter SR, et al. Oncogenic MITF dysregulation in clear cell sarcoma:

defining the MiT family of human cancers. Cancer Cell 2006;9:473–84.
18. Perera RM, Stoykova S, Nicolay BN, Ross KN, Fitamant J, Boukhali M, et al. Transcriptional control of autophagy-lysosome function drives pancreatic cancer metabolism. Nature 2015;524:361–5.
19. Valcarcel-Jimenez L, Macchia A, Martin-Martin N, Cortazar AR, Schaub-Clerigue A, Pujana-Vaquerizo M, et al. Integrative analysis of transcriptomics and clinical data uncovers the tumor-suppressive activity of MITF in prostate cancer. Cell Death Dis 2018;9:1041.
20. Fabbri L, Chakraborty A, Robert C, Vagner S. The plasticity of mRNA translation during cancer progression and therapy resistance. Nat Rev Cancer 2021;21:558–77.
21. Sendoel A, Dunn JG, Rodriguez EH, Naik S, Gomez NC, Hurwitz B, et al. Translation from unconventional 5′ start sites drives tumour initiation. Nature 2017;541:494–9.
22. Barna M, Pusic A, Zollo O, Costa M, Kondrashov N, Rego E, et al. Suppression of Myc oncogenic activity by ribosomal protein haploinsufficiency. Nature 2008;456:971–5.
23. Hsieh AC, Costa M, Zollo O, Davis C, Feldman ME, Testa JR, et al. Genetic dissection of the oncogenic mTOR pathway reveals druggable addiction to translational control via 4EBP-eIF4E. Cancer Cell 2010;17:249–61.
24. She QB, Halilovic E, Ye Q, Zhen W, Shirasawa S, Sasazuki T, et al. 4E-BP1 is a key effector of the oncogenic activation of the AKT and ERK signaling pathways that integrates their function in tumors. Cancer Cell 2010;18:39–51.
25. Wendel HG, De Stanchina E, Fridman JS, Malina A, Ray S, Kogan S, et al. Survival signalling by Akt and eIF4E in oncogenesis and cancer therapy. Nature 2004;428:332–7.
26. Furic L, Rong L, Larsson O, Koumakpayi IH, Yoshida K, Brueschke A, et al. eIF4E phosphorylation promotes tumorigenesis and is associated with prostate cancer progression. Proc Natl Acad Sci U S A 2010;107:14134–9.
27. Kwegyir-Afful AK, Bruno RD, Purushottamachar P, Murigi FN, Njar VC. Galeterone and VNPT55 disrupt Mnk-eIF4E to inhibit prostate cancer cell migration and invasion. FEBS J 2016;283:3898–918.
28. Bianchini A, Loiarro M, Bielli P, Busa R, Paronetto MP, Loreni F, et al. Phosphorylation of eIF4E by MNKs supports protein synthesis, cell cycle progression and proliferation in prostate cancer cells. Carcinogenesis 2008;29:2279–88.
29. Hsieh AC, Nguyen HG, Wen L, Edlind MP, Carroll PR, Kim W, et al. Cell type-specific abundance of 4EBP1 primes prostate cancer sensitivity or resistance to PI3K pathway inhibitors. Sci Signal 2015;8:ra116.
30. Hsieh AC, Liu Y, Edlind MP, Ingolia NT, Janes MR, Sher A, et al. The translational landscape of mTOR signalling steers cancer initiation and metastasis. Nature 2012;485:55–61.
31. Liu Y, Horn JL, Banda K, Goodman AZ, Lim Y, Jana S, et al. The androgen receptor regulates a druggable translational regulon in advanced prostate cancer. Sci Transl Med 2019;11:eaaw4993.
32. Masutani M, Sonenberg N, Yokoyama S, Imataka H. Reconstitution reveals the functional core of mammalian eIF3. EMBO J 2007;26:3373–83.
33. Wang H, Ru Y, Sanchez-Carbayo M, Wang X, Kieft JS, Theodorescu D. Translation initiation factor eIF3b expression in human cancer and its role in tumor growth and lung colonization. Clin Cancer Res 2013;19:2850–60.
34. Lee AS, Kranzusch PJ, Cate JH. eIF3 targets cell-proliferation messenger RNAs for translational activation or repression. Nature 2015;522:111–4.
35. Pulos-Holmes MC, Srole DN, Juarez MG, Lee AS, McSwiggen DT, Ingolia NT, et al. Repression of ferritin light chain translation by human eIF3. eLife 2019;8:e48193.
36. Fujii K, Zhulyn O, Byeon GW, Genuth NR, Kerr CH, Walsh EM, et al. Controlling tissue patterning by translational regulation of signaling transcripts through the core translation factor eIF3c. Dev Cell 2021;56:2928–37.
37. Lee AS, Kranzusch PJ, Doudna JA, Cate JH. eIF3d is an mRNA cap-binding protein that is required for specialized translation initiation. Nature 2016;536:96–9.
38. Reddy J, Fonseca MAS, Corona RI, Nameki R, Segato Dezem F, Klein IA, et al. Predicting master transcription factors from pan-cancer expression data. Sci Adv 2021;7:eabf6123.
39. Grasso CS, Wu YM, Robinson DR, Cao X, Dhanasekaran SM, Khan AP, et al. The mutational landscape of lethal castration-resistant prostate cancer. Nature 2012;487:239–43.
40. Taylor BS, Schultz N, Hieronymus H, Gopalan A, Xiao Y, Carver BS, et al. Integrative genomic profiling of human prostate cancer. Cancer Cell 2010;18:11–22.
41. Lapointe J, Li C, Higgins JP, van de Rijn M, Bair E, Montgomery K, et al. Gene expression profiling identifies clinically relevant subtypes of prostate cancer. Proc Natl Acad Sci U S A 2004;101:811–6.
42. Rotinen M, You S, Yang J, Coetzee SG, Reis-Sobreiro M, Huang WC, et al. ONECUT2 is a targetable master regulator of lethal prostate cancer that suppresses the androgen axis. Nat Med 2018;24:1887–98.
43. Aytes A, Mitrofanova A, Lefebvre C, Alvarez MJ, Castillo-Martin M, Zheng T, et al. Cross-species regulatory network analysis identifies a synergistic interaction between FOXM1 and CENPF that drives prostate cancer malignancy. Cancer Cell 2014;25:638–51.
44. Vidal SJ, Rodriguez-Bravo V, Quinn SA, Rodriguez-Barrueco R, Lujambio A, Williams E, et al. A targetable GATA2-IGF2 axis confers aggressiveness in lethal prostate cancer. Cancer Cell 2015;27:223–39.
45. Tuong ZK, Loudon KW, Berry B, Richoz N, Jones J, Tan X, et al. Resolving the immune landscape of human prostate at a single-cell level in health and cancer. Cell Rep 2021;37:110132.
46. Zong Y, Goldstein AS. Adaptation or selection–mechanisms of castration-resistant prostate cancer. Nat Rev Urol 2013;10:90–8.
47. Parham P, Ohta T. Population biology of antigen presentation by MHC class I molecules. Science 1996;272:67–74.
48. Doherty PC, Zinkernagel RM. A biological role for the major histocompatibility antigens. Lancet 1975;1:1406–9.
49. Camacho L, Zabala-Letona A, Cortazar AR, Astobiza I, Dominguez-Herrera A, Ercilla A, et al. Identification of androgen receptor metabolic correlome reveals the repression of ceramide kinase by androgens. Cancers 2021;13:4307.
50. Cancer Genome Atlas Research Network. The molecular taxonomy of primary prostate cancer. Cell 2015;163:1011–25.
51. Fraser M, Sabelnykova VY, Yamaguchi TN, Heisler LE, Livingstone J, Huang V, et al. Genomic hallmarks of localized, non-indolent prostate cancer. Nature 2017;541:359–64.
52. Williams ES, Rodriguez-Bravo V, Chippada-Venkata U, De Ia Iglesia-Vicente J, Gong Y, Galsky M, et al. Generation of prostate cancer patient-derived xenograft models from circulating tumor cells. J Vis Exp 2015:53182.
53. Zhang J, Huang D, Saw PE, Song E. Turning cold tumors hot: from molecular mechanisms to clinical applications. Trends Immunol 2022;43:523–45.
54. Montesion M, Murugesan K, Jin DX, Sharaf R, Sanchez N, Guria A, et al. Somatic HLA class I loss is a widespread mechanism of immune evasion which refines the use of tumor mutational burden as a biomarker of checkpoint inhibitor response. Cancer Discov 2021;11:282–92.
55. Chowell D, Morris LGT, Grigg CM, Weber JK, Samstein RM, Makarov V, et al. Patient HLA class I genotype influences cancer response to checkpoint blockade immunotherapy. Science 2018;359:582–7.
56. Gu SS, Zhang W, Wang X, Jiang P, Traugh N, Li Z, et al. Therapeutically increasing MHC-I expression potentiates immune checkpoint blockade. Cancer Discov 2021;11:1524–41.
57. Ennishi D, Takata K, Beguelin W, Duns G, Mottok A, Farinha P, et al. Molecular and genetic characterization of MHC deficiency identifies EZH2 as therapeutic target for enhancing immune recognition. Cancer Discov 2019;9:546–63.
58. Burr ML, Sparbier CE, Chan KL, Chan YC, Kersbergen A, Lam EYN, et al. An evolutionarily conserved function of polycomb silences the MHC class I antigen presentation pathway and enables immune evasion in cancer. Cancer Cell 2019;36:385–401.
59. Yamamoto K, Venida A, Yano J, Biancur DE, Kakiuchi M, Gupta S, et al. Autophagy promotes immune evasion of pancreatic cancer by degrading MHC-I. Nature 2020;581:100–5.

60. Abida W, Cyrta J, Heller G, Prandi D, Armenia J, Coleman I, et al. Genomic correlates of clinical outcome in advanced prostate cancer. Proc Natl Acad Sci U S A 2019;116:11428–36.
61. Takemura R, Takaki H, Okada S, Shime H, Akazawa T, Oshiumi H, et al. PolyI:C-induced, TLR3/RIP3-dependent necroptosis backs up immune effector-mediated tumor elimination in vivo. Cancer Immunol Res 2015;3:902–14.
62. Amos SM, Pegram HJ, Westwood JA, John LB, Devaud C, Clarke CJ, et al. Adoptive immunotherapy combined with intratumoral TLR agonist delivery eradicates established melanoma in mice. Cancer Immunol Immunother 2011;60:671–83.
63. Moerke NJ, Aktas H, Chen H, Cantel S, Reibarkh MY, Fahmy A, et al. Small-molecule inhibition of the interaction between the translation initiation factors eIF4E and eIF4G. Cell 2007;128:257–67.
64. Fizazi K, Tran N, Fein L, Matsubara N, Rodriguez-Antolin A, Alekseev BY, et al. Abiraterone plus prednisone in metastatic, castration-sensitive prostate cancer. N Engl J Med 2017;377:352–60.
65. James ND, de Bono JS, Spears MR, Clarke NW, Mason MD, Dearnaley DP, et al. Abiraterone for prostate cancer not previously treated with hormone therapy. N Engl J Med 2017;377:338–51.
66. Armstrong AJ, Szmulewitz RZ, Petrylak DP, Holzbeierlein J, Villers A, Azad A, et al. ARCHES: a randomized, phase III study of androgen deprivation therapy with enzalutamide or placebo in men with metastatic hormone-sensitive prostate cancer. J Clin Oncol 2019;37:2974–86.
67. Zhang L, Pan X, Hershey JW. Individual overexpression of five subunits of human translation initiation factor eIF3 promotes malignant transformation of immortal fibroblast cells. J Biol Chem 2007;282:5790–800.
68. de la Parra C, Ernlund A, Alard A, Ruggles K, Ueberheide B, Schneider RJ. A widespread alternate form of cap-dependent mRNA translation initiation. Nat Commun 2018;9:3068.
69. Chen CD, Welsbie DS, Tran C, Baek SH, Chen R, Vessella R, et al. Molecular determinants of resistance to antiandrogen therapy. Nat Med 2004;10:33–9.
70. Lamont KR, Tindall DJ. Minireview: alternative activation pathways for the androgen receptor in prostate cancer. Mol Endocrinol 2011;25:897–907.
71. Fujita K, Nonomura N. Role of androgen receptor in prostate cancer: a review. World J Mens Health 2019;37:288–95.
72. Leung JK, Sadar MD. Non-genomic actions of the androgen receptor in prostate cancer. Front Endocrinol 2017;8:2.
73. Venkatachalam S, McFarland TR, Agarwal N, Swami U. Immune checkpoint inhibitors in prostate cancer. Cancers 2021;13:2187.
74. Xu Y, Poggio M, Jin HY, Shi Z, Forester CM, Wang Y, et al. Translation control of the immune checkpoint in cancer and its therapeutic targeting. Nat Med 2019;25:301–11.
75. Cerezo M, Guemiri R, Druillennec S, Girault I, Malka-Mahieu H, Shen S, et al. Translational control of tumor immune escape via the eIF4F-STAT1-PD-L1 axis in melanoma. Nat Med 2018;24:1877–86.
76. Suresh S, Chen B, Zhu J, Golden RJ, Lu C, Evers BM, et al. eIF5B drives integrated stress response-dependent translation of PD-L1 in lung cancer. Nat Cancer 2020;1:533–45.
77. Guan X, Polesso F, Wang C, Sehrawat A, Hawkins RM, Murray SE, et al. Androgen receptor activity in T cells limits checkpoint blockade efficacy. Nature 2022;606:791–6.
78. Gamat M, McNeel DG. Androgen deprivation and immunotherapy for the treatment of prostate cancer. Endocr Relat Cancer 2017;24:T297–310.
79. Zhu Y, Duong L, Lu X, Lu X. Cancer-cell-intrinsic mechanisms shaping the immunosuppressive landscape of prostate cancer. Asian J Androl 2023;25:171–8.
80. Abdel-Hafiz HA, Schafer JM, Chen X, Xiao T, Gauntner TD, Li Z, et al. Y chromosome loss in cancer drives growth by evasion of adaptive immunity. Nature 2023;619:624–31.
81. Rambow F, Marine JC, Goding CR. Melanoma plasticity and phenotypic diversity: therapeutic barriers and opportunities. Genes Dev 2019;33:1295–318.
82. Du J, Miller AJ, Widlund HR, Horstmann MA, Ramaswamy S, Fisher DE. MLANA/MART1 and SILV/PMEL17/GP100 are transcriptionally regulated by MITF in melanocytes and melanoma. Am J Pathol 2003;163:333–43.
83. Ho JJD, Cunningham TA, Manara P, Coughlin CA, Arumov A, Roberts ER, et al. Proteomics reveal cap-dependent translation inhibitors remodel the translation machinery and translatome. Cell Rep 2021;37:109806.
84. Nakagawa S, Wei L, Song WM, Higashi T, Ghoshal S, Kim RS, et al. Molecular liver cancer prevention in cirrhosis by organ transcriptome analysis and lysophosphatidic acid pathway inhibition. Cancer Cell 2016;30:879–90.
85. Jin HJ, Kim J, Yu J. Androgen receptor genomic regulation. Transl Androl Urol 2013;2:157–77.
86. Massie CE, Lynch A, Ramos-Montoya A, Boren J, Stark R, Fazli L, et al. The androgen receptor fuels prostate cancer by regulating central metabolism and biosynthesis. EMBO J 2011;30:2719–33.
87. Cortazar AR, Torrano V, Martin-Martin N, Caro-Maldonado A, Camacho L, Hermanova I, et al. CANCERTOOL: a visualization and representation interface to exploit cancer datasets. Cancer Res 2018;78:6320–8.
88. Mariathasan S, Turley SJ, Nickles D, Castiglioni A, Yuen K, Wang Y, et al. TGFbeta attenuates tumour response to PD-L1 blockade by contributing to exclusion of T cells. Nature 2018;554:544–8.
89. Powles T, Yuen KC, Gillessen S, Kadel EE 3rd, Rathkopf D, Matsubara N, et al. Atezolizumab with enzalutamide versus enzalutamide alone in metastatic castration-resistant prostate cancer: a randomized phase 3 trial. Nat Med 2022;28:144–53.
90. Ovcharenko I, Loots GG, Giardine BM, Hou M, Ma J, Hardison RC, et al. Mulan: multiple-sequence local alignment and visualization for studying function and evolution. Genome Res 2005;15:184–94.
91. Dreos R, Ambrosini G, Perier RC, Bucher P. The eukaryotic promoter database: expansion of EPDnew and new promoter analysis tools. Nucleic Acids Res 2015;43:D92–6.
92. Dhital B, Santasusagna S, Kirthika P, Xu M, Li P, Carceles-Cordon M, et al. Harnessing transcriptionally driven chromosomal instability adaptation to target therapy-refractory lethal prostate cancer. Cell Rep Med 2023;4:100937.
93. Rodriguez-Bravo V, Pippa R, Song WM, Carceles-Cordon M, Dominguez-Andres A, Fujiwara N, et al. Nuclear pores promote lethal prostate cancer by increasing POM121-driven E2F1, MYC, and AR nuclear import. Cell 2018;174:1200–15.
94. Van Nostrand EL, Nguyen TB, Gelboin-Burkhart C, Wang R, Blue SM, Pratt GA, et al. Robust, cost-effective profiling of RNA binding protein targets with single-end enhanced crosslinking and immunoprecipitation (seCLIP). Methods Mol Biol 2017;1648:177–200.
95. Kivioja T, Vaharautio A, Karlsson K, Bonke M, Enge M, Linnarsson S, et al. Counting absolute numbers of molecules using unique molecular identifiers. Nat Methods 2011;9:72–4.
96. Smith T, Heger A, Sudbery I. UMI-tools: modeling sequencing errors in unique molecular identifiers to improve quantification accuracy. Genome Res 2017;27:491–9.
97. Hubley R, Finn RD, Clements J, Eddy SR, Jones TA, Bao W, et al. The Dfam database of repetitive DNA families. Nucleic Acids Res 2016;44:D81–9.
98. Benson DA, Cavanaugh M, Clark K, Karsch-Mizrachi I, Lipman DJ, Ostell J, et al. GenBank. Nucleic Acids Res 2013;41:D36–42.
99. Dobin A, Davis CA, Schlesinger F, Drenkow J, Zaleski C, Jha S, et al. STAR: ultrafast universal RNA-seq aligner. Bioinformatics 2013;29:15–21.
100. Lovci MT, Ghanem D, Marr H, Arnold J, Gee S, Parra M, et al. Rbfox proteins regulate alternative mRNA splicing through evolutionarily conserved RNA bridges. Nat Struct Mol Biol 2013;20:1434–42.
101. Frankish A, Diekhans M, Ferreira AM, Johnson R, Jungreis I, Loveland J, et al. GENCODE reference annotation for the human and mouse genomes. Nucleic Acids Res 2019;47:D766–D73.
102. Zhao Y, Ding L, Wang D, Ye Z, He Y, Ma L, et al. EZH2 cooperates with gain-of-function p53 mutants to promote cancer growth and metastasis. EMBO J 2019;38:e99599.

103. Shen S, Faouzi S, Bastide A, Martineau S, Malka-Mahieu H, Fu Y, et al. An epitranscriptomic mechanism underlies selective mRNA translation remodelling in melanoma persister cells. Nat Commun 2019;10:5713.
104. Schmidt EK, Clavarino G, Ceppi M, Pierre P. SUnSET, a nonradioactive method to monitor protein synthesis. Nat Methods 2009;6:275–7.
105. Goodman CA, Hornberger TA. Measuring protein synthesis with SUnSET: a valid alternative to traditional techniques? Exerc Sport Sci Rev 2013;41:107–15.
106. Fellmann C, Hoffmann T, Sridhar V, Hopfgartner B, Muhar M, Roth M, et al. An optimized microRNA backbone for effective single-copy RNAi. Cell Rep 2013;5:1704–13.
107. Hershey CL, Fisher DE. Genomic analysis of the microphthalmia locus and identification of the MITF-J/Mitf-J isoform. Gene 2005; 347:73–82.
108. He Y, Wang L, Wei T, Xiao YT, Sheng H, Su H, et al. FOXA1 overexpression suppresses interferon signaling and immune response in cancer. J Clin Invest 2021;131:e147025.